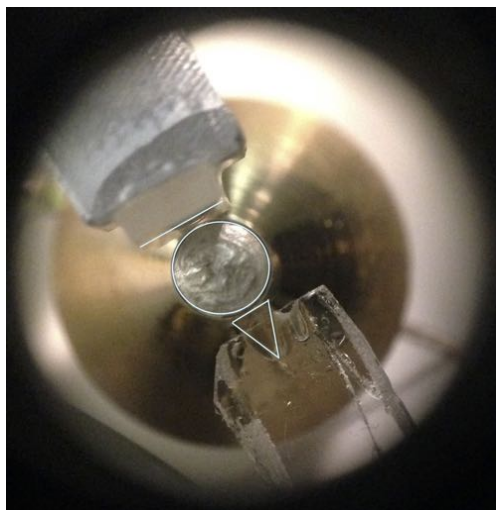

WHISPERING-GALLERY MODE SHIFTS WITH DIELECTRIC MATERIALS IN THE EVANESCENT FIELD OF A RESONATOR



Author :

NAVID SOLTANI

Supervisors :

Dr. CHRISTOPH MARQUARDT
Prof. ARNO RAUSCHENBEUTEL

March 20, 2016

Abstract

The resonance frequencies of whispering gallery mode resonator (WGMR) are affected by various parameters such as temperature, pressure or an interaction of a dielectric material with the evanescent of the WGMs.

Here, we investigate a frequency detuning method based on moving a dielectric substrate towards the WGMR. As long as the dielectric substrate has not touched the resonator, the detuning will undergo an exponential change as the distance decreases. This technique can be used for dielectric material analysis and sensing due to the shifts of the whispering gallery modes.

Furthermore, if the dielectric substrate applies a pressure on the WGMR, it can change the mode frequency in the range of few GHz. We characterize this tuning method and its potential use as a continuous frequency tuning mechanism for nonlinear optical processes in the WGMR.

Contents

1	Introduction	1
2	Theoretical background	3
2.1	Basics of electrodynamics	3
2.1.1	The Maxwell's and wave equations	3
2.1.2	Material equations	4
2.1.3	Nonlinear optics	6
2.2	Properties of lithium niobate	7
2.2.1	Sellmeier equation	7
2.2.2	Thermal expansion	8
2.2.3	Elasticity	8
2.3	Whispering-gallery resonators	9
2.3.1	Field build-up in resonator	10
2.3.2	Mode spectrum	13
2.3.3	Evanescent field coupling	16
2.3.4	Parametric down conversion	18
2.3.5	Temperature tuning of the mode spectrum	20
2.3.6	Pressure tuning of the mode spectrum	22
2.3.7	Frequency shifts induced by a dielectric coupler	24
3	Experimental setup	27
3.1	Fabrication of whispering-gallery resonator	27
3.2	Experimental scheme	28
3.3	Calibration of the Attocube positioner	31
3.4	Measurement of the contact point	32
3.5	Design of the setup chamber	34
4	Results and discussion	35
4.1	Temperature stabilization with TE and TM modes	35
4.2	Towards parametric down conversion using blue light	39
4.3	Frequency tuning of whispering-gallery modes	40
4.3.1	Local temperature variations	41
4.3.2	Frequency shifts at room temperature	42
4.3.3	Pressure tuning by movable dielectric substrate	47
4.3.4	Evanescent field tuning by movable dielectric substrate	49

5 Conclusion and outlook	53
Acknowledgments	55
Bibliography	59

Chapter 1

Introduction

Biological and mechanical sensing applications using microcavities have drawn increasing attention over the recent years [1]. Due to high sensitivity and small size of microcavities, they are a good candidate for sensing and can have many industrial applications. Furthermore, the ability of fine resonance frequency tuning in these cavities make them suitable to match the atomic transitions or lock the laser frequencies.

Whispering gallery mode resonators (WGMR) are a kind of optical microcavities which confines light via total internal reflection. The interaction with the surrounding medium by the evanescent field which is coming out of the resonator can be used for sensing applications or tuning the resonance frequency. In mechanical tuning and sensing applications, a small change in the geometry of the microsphere causes a shift in the resonance frequency. Such frequency shifts can be measured optically with very high precision [2, 3]. State of the art experiments achieve a resolution limit down to detecting single molecules [4, 5] or proteins [6].

The high quality factors and the wavelength independent nature of total internal reflection make WGMRs an ideal candidate for nonlinear optics. Moreover, lithium niobate has a high $\chi^{(2)}$ nonlinearity which can be a suitable host material in WGMRs. Parametric down conversion (PDC), where one pump photons decay into one pair of signal and idler photons, is one of the wide applications of WGMRs made of lithium niobate [7, 8]. Due to energy conservation, a set of tuning mechanisms based on the mode analysis of the WGMR spectrum at the pump wavelength can be used for precise tuning of the frequency of signal and idler. One way to tune the resonance frequency is changing the temperature of crystal. With only the temperature tuning, one is limited to discrete solutions of the phase-matching conditions. Continuous tuning of the parametric frequencies on the MHz scale is achieved by pressure tuning and manipulating the evanescent fields [9].

In this thesis we investigate the resonance frequency shifts of different WGMR via movable dielectric substrates. The dielectric can change the resonance frequency by interacting with WGR evanescent field or by applying mechanical pressuring the resonator. The temperature tuning as a discrete frequency tuning and temperature stabilization with different TE and TM mode shifts is also considered. This study can provide the precise continuous wavelength tuning over 100 nm of both modes with controllable bandwidth between 7.2 and 13 MHz for a WGR single photon sources [10]. The experimental results show that the

distance of coupling prism with the resonator can affect the mode shifts differently. This should be considered in mode analysis as a factor of evanescent field interactions.

This thesis is structured as follows. The second chapter shows the theoretical overview of electromagnetic field in WGR and describes briefly the properties of lithium niobate as a material for the WGR. In the third chapter, we describe the different parts of the experimental setup. Furthermore, we demonstrate our resonator fabrication techniques and introduce a portable vacuum chamber design for a next generation of WGR setup. In the fourth part we show results on the the stability of the system and the resonance frequency shifts due to movable dielectric substrate. In fifth chapter we draw our conclusions and elaborate on future plans.

Chapter 2

Theoretical background

This chapter describes the theories which supports the experimental results. The first section generally describes the electromagnetic wave with Maxwell's equations and the wave equation. The second section is about lithium niobate properties, the material which the WGMR is made of it in this project. The third section will introduce our micro-cavity resonator called whispering gallery mode resonator and describes its features.

2.1 Basics of electrodynamics

Starting from Maxwell's equation in vacuum as the simplest system and continuing with the effect of a material on electromagnetic wave propagating toward it is the goal of this section. The nonlinear response of the medium which can affect the properties of light is considered in the last part.

2.1.1 The Maxwell's and wave equations

An electromagnetic field is described by the electric vector field $\vec{E}(r, t)$ and the magnetic field $\vec{B}(r, t)$ that are functions of position and time. Therefore, six scalar functions of position and time are required to describe light in free space. But these functions are interrelated by the Maxwell's equations [11]. The homogeneous Maxwell's equations are:

$$\nabla \cdot \vec{B} = 0, \quad (2.1a)$$

$$\nabla \times \vec{E} = -\frac{\partial \vec{B}}{\partial t}, \quad (2.1b)$$

and the inhomogeneous Maxwell's equations are described as:

$$\nabla \cdot \vec{E} = \frac{\rho}{\epsilon_0}, \quad (2.2a)$$

$$\nabla \times \vec{B} = \mu_0 j + \frac{1}{c^2} \frac{\partial \vec{E}}{\partial t}, \quad (2.2b)$$

Which, ϵ_0 and μ_0 are permittivity and permeability in vacuum, respectively. ρ is the charge density and j is the current density. Considering electromagnetic wave in vacuum, ρ and j are zero and $c = 1/\sqrt{\epsilon_0\mu_0}$ is the speed of light. The wave equation in vacuum can be derived from Maxwell's equations by applying the curl operation ($\nabla \times$) to Eq.(2.1b) and using the vector identity relation ($\nabla \times (\nabla \times \vec{E}) = \nabla(\nabla \cdot \vec{E}) - \nabla^2 \vec{E}$). Then with substitution of Eq.(2.2b) for $j = 0$ one reaches to:

$$\nabla \times (\nabla \times \vec{E}) + \nabla \times \frac{\partial \vec{B}}{\partial t} = -\nabla^2 \vec{E} + \frac{1}{c^2} \frac{\partial^2 \vec{E}}{\partial t^2} = 0. \quad (2.3)$$

The right side of Eq.(2.3) is known as wave equation. In general case the wave equation can be written as:

$$-\nabla^2 u + \frac{1}{c^2} \frac{\partial^2 u}{\partial t^2} = 0, \quad (2.4)$$

where u is a scalar function with components of \vec{E} and \vec{B} . Eq.(2.4) can be solved in different boundary conditions to limit the problem to a discrete set of eigenstates.

2.1.2 Material equations

For the description of electromagnetic field in medium, a macroscopic approach is used to explain the effects of many single particles interact with field. In this case the electric field \vec{E} and magnetic field \vec{B} are related to the displacement field \vec{D} and magnetizing field \vec{H} , respectively.

$$\vec{D}(t) = \epsilon_0 \vec{E} + \vec{P}, \quad (2.5a)$$

$$\vec{B}(t) = \mu_0 \vec{H} + \vec{M}. \quad (2.5b)$$

In linear optics, the polarization density \vec{P} depends linearly upon the electric field strength and described by:

$$\vec{P} = \chi^{(1)} \vec{E}, \quad (2.6)$$

where $\chi^{(1)}$ is known as the first order susceptibility and is scalar for isotropic materials. $\chi^{(1)}$ defines materials relative permittivity (ϵ_r) and velocity of electromagnetic wave in medium.

$$\epsilon_r = \epsilon_0(1 + \chi^{(1)}), \quad (2.7)$$

$$c' = \frac{1}{\epsilon_r \mu_r} = \frac{c}{n}, \quad (2.8)$$

which c' is the phase velocity of the wave, μ_r is the relative permeability and n is the refractive index which can be different depends on direction and polarization of light in an anisotropic crystals.

For anisotropic materials, the polarization density and the electric field are generally not in the same direction. The relation between the vector \vec{P} and \vec{E} depends on the direction of the vector \vec{E} and is written as [11]:

$$P_i = \sum_j \epsilon_0 \chi_{ij} E_j, \quad (2.9)$$

for linear, nondispersive and homogeneous medium. The indexes $i, j = 1, 2, 3$ donate the x, y and z components, respectively. The dielectric properties of the medium are then described by 3×3 array of χ_{ij} and form the electric susceptibility tensor χ . A similar relation between D and E applies:

$$D_i = \sum_j \epsilon_{ij} E_j, \quad (2.10)$$

which ϵ_{ij} are elements of the electric permittivity tensor.

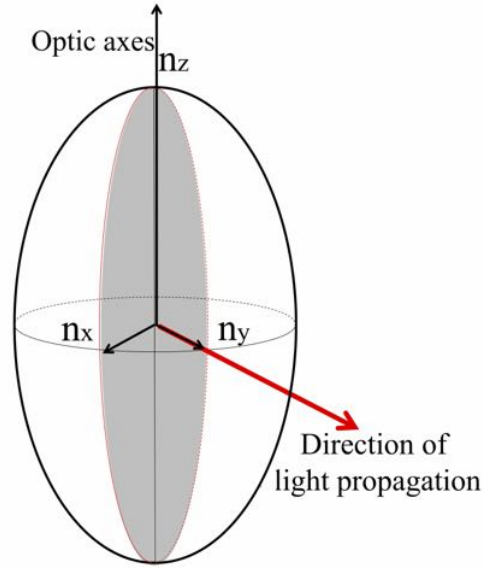


Figure 2.1: Basic example of using the ellipsoid to analyze propagation along the y axes in a z cut lithium niobate and $n_x = n_y$. The n_x and n_z define the refractive index for p and s polarized light, respectively.

Energy conservation rule and time reversal symmetry, show that the ϵ_{ij} is a symmetric matrix. According to linear algebra, any symmetric matrix can be diagonalized by a suitable choice of the basis vectors, ϵ_{ij} can be written as diagonal matrix. With this choice for the basis (called coordinate axes) one can write Eq.(2.10) for nonmagnetic and transparent material as:

$$\begin{bmatrix} D_x \\ D_y \\ D_z \end{bmatrix} = \epsilon_0 \begin{bmatrix} n_x^2 & 0 & 0 \\ 0 & n_y^2 & 0 \\ 0 & 0 & n_z^2 \end{bmatrix} \begin{bmatrix} E_x \\ E_y \\ E_z \end{bmatrix}$$

where $\epsilon_{ii} = \epsilon_0 n_i^2$. Here the energy density equation is:

$$U = \frac{1}{2} \vec{E} \cdot \vec{D} = \frac{1}{2} \left[\frac{D_x^2}{\epsilon_0 n_x^2} + \frac{D_y^2}{\epsilon_0 n_y^2} + \frac{D_z^2}{\epsilon_0 n_z^2} \right], \quad (2.11)$$

and it can be written as an ellipsoid equation.

$$\frac{\alpha_x^2}{n_x^2} + \frac{\alpha_y^2}{n_y^2} + \frac{\alpha_z^2}{n_z^2} = 1, \quad (2.12)$$

which $\vec{\alpha} = (\vec{D}/\sqrt{2\epsilon_0\vec{U}})^2$. This ellipsoid can describe the crystal refractive index in any direction and called index ellipsoid. The optic axis is an orthogonal axes to the circle cross section of this ellipsoid. (shown in Fig.2.1). Generally, crystals have three principal refractive indices. If all the three indices are the same, the medium is characterized as isotropic ($n_x = n_y = n_z$); if two of them are the same, is characterized as uniaxial ($n_x = n_y \neq n_z$); and if all three are different, is called biaxial ($n_x \neq n_y \neq n_z$). Uniaxial has one optical axes but biaxial has two.

In optics, dispersion is a phenomena in which the phase velocity of a wave depends on its frequency. The media having this property is a dispersive media. In such a media the relation between the vectors \vec{P} and \vec{E} is dynamic rather than instantaneous [11]. The presence of a time between the input and output vector can change the $P(t)$ (see Fig.2.2). For linear and isotropic materials the dynamic relation between arbitrary electron field $\vec{E}(t)$ and polarization density $\vec{P}(t)$ can be expressed as a convolution for $t' \leq t$:

$$\vec{P}(t) = \epsilon_0 \int_{-\infty}^{\infty} \chi(t-t')\vec{E}(t')dt'. \quad (2.13)$$

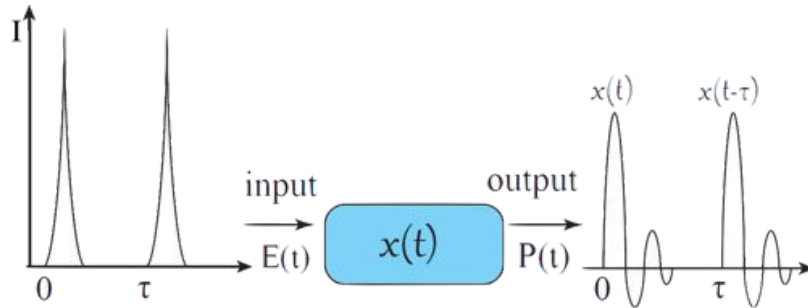


Figure 2.2: Response of a linear shift-invariant system to pulses in a dispersive media

Alternatively, a dynamic linear system may be described by its transfer function. As an example, the transfer function at frequency ν is $\epsilon_0\chi(\nu)$, where $\chi(\nu)$ is the Fourier transform of $\chi(t)$ so that it is frequency-dependent susceptibility.

2.1.3 Nonlinear optics

Nonlinear optics is the study of phenomena that occur as a consequence of the modification of the optical properties of a material system by presence of light [12]. The beginning of nonlinear optics is widely considered to be the discovery of second-harmonic generation by Franken et al. in 1961 which is basically inversion of parametric down conversion (PDC)

process presented in section (2.3.4). In nonlinear optics Eq.(2.6) can be generalized by expressing the polarization \vec{P} as a power series in the electric field \vec{E} as:

$$\begin{aligned}\vec{P} &= \chi^{(1)}\vec{E} + \chi^{(2)}\vec{E}^2 + \chi^{(3)}\vec{E}^3 + \dots \\ &\equiv \vec{P}^{(1)} + \vec{P}^{(2)} + \vec{P}^{(3)} + \dots\end{aligned}\quad (2.14)$$

The quantities $\chi^{(2)}$ and $\chi^{(3)}$ are known as the second and third order nonlinear optical susceptibilities, respectively. Furthermore, the displacement field can be written as $\vec{D} = \vec{D}^{(1)} + \vec{D}^{(2)} + \vec{D}^{(3)} + \dots$ regarding to Eq.(2.5a).

By the divergence theorem, Gauss's law for the field \vec{P} can be stated as

$$\nabla \cdot \vec{P} = -\rho, \quad (2.15)$$

where $\partial \vec{P} / \partial t = \vec{j}$. This indicates that the wave function in nonlinear, nonmagnetic ($\vec{M} = 0$) media can be written as:

$$\begin{aligned}\nabla(\nabla \cdot E) - \nabla^2 E &= -\frac{1}{c^2} \frac{\partial^2 E}{\partial t^2} - \mu_0 \frac{\partial^2 P}{\partial t^2} \\ \nabla^2 E - \frac{1}{c^2} \frac{\partial^2 E}{\partial t^2} &= \mu_0 \frac{\partial^2 P}{\partial t^2}.\end{aligned}\quad (2.16)$$

Eq.(2.16) is valid for all homogeneous and isotropic media.

2.2 Properties of lithium niobate

Uniaxial and biaxial (see section 2.1.2) crystals present the interesting and counterintuitive property of two different indices of refraction on the electromagnetic's wave direction of propagation and polarization state. This physical property is known as birefringence. Optical waveplates, beam splitters, and group velocity delay compensation plates are only a few of the optical devices whose operation is based on birefringence. In this section we describe some properties of lithium niobate as a widely used uniaxial crystal. The WGMR in our experiment is made of z-cut lithium niobate.

2.2.1 Sellmeier equation

The Sellmeier equation is an empirical relationship between the refractive index and wavelength for a particular transparent medium. It is used to determine the dispersion of light in the medium. The Sellmeier equation for Lithium niobate with magnesium doping is defined as: [13]

$$n_i^2 = \frac{A_{0,i} + A_{NbLi} c_{NbLi} + A_{Mg,i} c_{Mg}}{(\lambda_{0,i} + \mu_{0,i} F)^{-2} - \lambda - 2} - A_{IR,i} \lambda^2 + A_{UV}, \quad (2.17)$$

where λ is the wavelength and $F = f(T) - f(T_0)$ is a temperature dependent with:

$$f(T) = (T + 273)^2 + 4.023 \times 10^5 \left[\coth\left(\frac{261.6}{T + 273}\right) - 1 \right]. \quad (2.18)$$

The other values are constant and mentioned in Ref. [14]. Based on Eq.(2.17, 2.18), the refractive index also depends on temperature.

2.2.2 Thermal expansion

Axial expansion of lithium niobate due to temperature variation is described by the thermal expansion coefficient α [15]:

$$\alpha = a(1 + bT + cT^2 + dT^3). \quad (2.19)$$

This is an empirical equation and obtained from the third-order polynomial fit to the experimental data. The coefficients in this equation have values of $a = 5.14$, $b = 13.43 \times 10^{-6}$, $c = 17.55 \times 10^{-9}$ and $d = 16.3 \times 10^{-12}$ at room temperature. The results of this equation is in Angstrom (e.g. $\alpha = 5.151 \text{ \AA}$ at 298 K). The expansion has a different value for different axis regarding the crystal structure.

2.2.3 Elasticity

The elasticity of a solid can be described by the strain in the material that results from a mechanically applied stress. This relationship is linear and is represented by Hooke's law [16],

$$S_{ij} = \sum_{kl} c_{ijkl} \sigma_{kl}, \quad (2.20)$$

where S_{ij} is the strain tensor and σ_{kl} is the stress tensor. c_{ijkl} is the fourth-order stiffness tensor. A reciprocal expression can also be written as

$$\sigma_{ij} = \sum_{kl} s_{ijkl} S_{kl}, \quad (2.21)$$

which s_{ijkl} is the elastic compliance. If body torques are ignored, it can be shown that $s_{ijkl} = s_{ijlk} = s_{jikl}$ [17]. With this relation the 81 elements tensor is reduced to 36 independent elements. Since the lithium niobate crystal possesses $3m$ point group symmetry, all tensors describing the physical properties of lithium niobate must follow this symmetry. This basic principle was first asserted by Neumann in 1833 [18]. As a result, the elastic compliance ends up with 6×6 matrix:

$$s = \begin{bmatrix} s_{11} & s_{12} & s_{13} & s_{14} & 0 & 0 \\ s_{12} & s_{11} & s_{13} & -s_{14} & 0 & 0 \\ s_{13} & s_{13} & s_{33} & 0 & 0 & s_0 \\ s_{14} & -s_{14} & 0 & s_{44} & 0 & 0 \\ 0 & 0 & 0 & 0 & s_{44} & 2s_{14} \\ 0 & 0 & 0 & 0 & 2s_{14} & 2(s_{11} - s_{12}) \end{bmatrix}$$

which has only 6 independent parameters and the values for constant electric field are shown in table 2.1.

s_{11}	s_{12}	s_{13}	s_{14}	s_{33}	s_{44}	Ref
5.83	-1.15	-1.45	-1.00	5.02	17.10	[19]
5.78	-1.01	-1.47	-1.02	5.02	17.00	[16]

Table 2.1: Elastic compliance coefficient $[\times 10^{-12} \text{ m}^2/\text{N}]$ at constant electric field in LiNbO_3

2.3 Whispering-gallery resonators

In the first part of 20th century numerous studies were conducted on optical micro cavities with different structures. One of these cavities with cylindrical, spherical or toroid shape is whispering-gallery resonators (WGR) was discovered by W. W. Hansen [20].

Whispering-gallery waves were explained for sound waves by Lord Rayleigh in 1878 before discovery of optical WGR. Rayleigh discovered that sound waves can travel on the wall's of the St Paul's Cathedral dome (Fig.2.3.a is a picture of the dome). This was a revision to a previous misconception; whispers could be heard across the dome but not at any intermediate position.

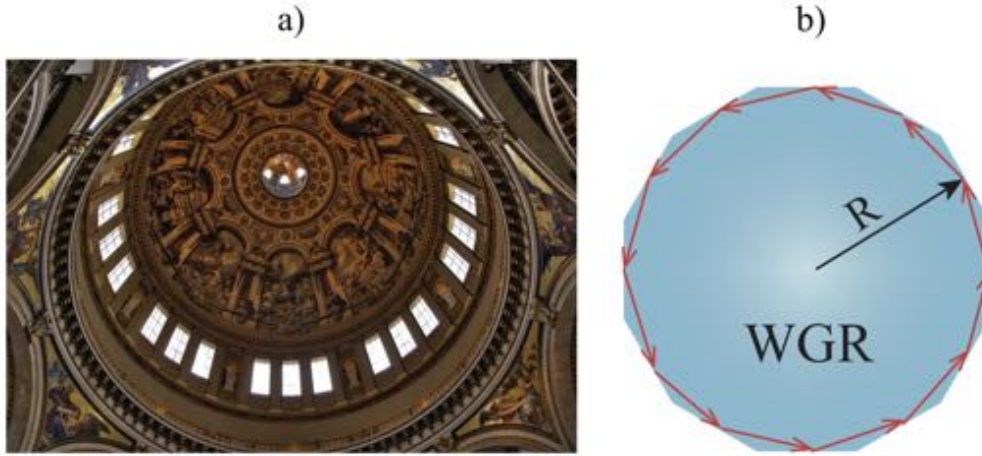


Figure 2.3: a) Dome of St Paul's Cathedral in London with acoustic whispering-gallery property. The image is taken from Ref. [21]. b) Top view of whispering-gallery resonator with radius R . The light is confined inside the resonator due to total internal reflection.

In whispering gallery resonators the light circling around the cavity, supported by continuous total internal reflection of the cavity surface (see Fig.2.3.b). After one round trip the light can return to the same point with the same phase and hence interfere constructively with themselves, forming standing waves that trapped inside the cavity [22]. Due to their small size, high transmittance and narrow bandwidth of the cavity resonance they are a suitable candidate for vast range of applications such as: tunable single photon source [10], single-particle sensing [1], narrow-band optical filtering [23], temperature measurement and

stabilization [24], pressure measurement [25], different phenomena of nonlinear interactions (such as wave mixing and Raman and parametric scattering) [26, 27].

2.3.1 Field build-up in resonator

WGRs can be modeled as linear cavities, which consist of two mirrors aligned on one optical axis. They exactly retro-reflect the incident light beam (see Fig.2.4). The optical path length in a linear cavity is derived from the round trip of light in cavity with length d and inner refractive index n at a certain wavelength λ_0 . Whenever the optical path matches the multiple of its wavelength, a constructive interference occurs:

$$m\lambda_0 = 2dn. \quad (2.22)$$

where m is the integer number of wavelengths who covers the resonator length, λ_0 is the light wavelength inside the resonator, d is the resonator length and n is the refractive index of media inside the resonator. If an electromagnetic field E_{in} with frequency ν impinges

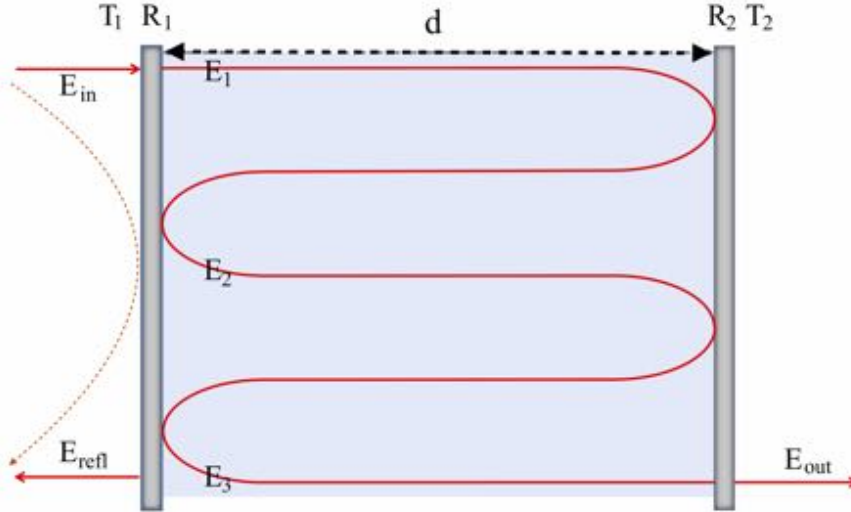


Figure 2.4: Linear resonator with an inner refractive index n and two end mirrors with different intensity reflectivities R_1 and R_2 . The transmission of an incoming electric wave with amplitude E_{in} can constructively interfere in resonance frequency.

on the first mirror, it gets partly reflected and transmitted. R_i and T_i ($i = 1, 2$) are the reflectivity and transmissivity, respectively. The transmitted part is $E_0 = \sqrt{T_1^{cav}} E_{in}$ and after each round trip, the amplitude E_j ($j \in \mathbb{N}$) of the electric field is attenuated due to medium absorption α_x and transmission through both mirrors. The electromagnetic field experiences a phase shift of $\phi = 2\pi(\nu - \nu_0)(2nd/c)$ which $\nu_0 = c/\lambda_0$ is the central resonance frequency [28]. All these effects are shown with frequency dependent feedback parameter $g(\nu)$.

$$E_{j+1} = g(\nu).E_j = \sqrt{R_1^{cav}.R_2^{cav}} e^{2d\alpha_x}.e^{i\phi}.E_j. \quad (2.23)$$

At the end the amplitude of the electric field inside and outside the cavity and reflected is:

$$\begin{aligned}
 E_{cav} &= (1 + g(\nu) + g^2(\nu) + g^3(\nu) + \dots) E_0 \stackrel{\text{geometric series}}{=} \frac{1}{1 - g(\nu)} E_0 \\
 &= E_{in} \frac{\sqrt{T_1^{cav}}}{1 - \sqrt{R_1^{cav} \cdot R_2^{cav}} e^{2d\alpha_x} \cdot e^{i\phi}}, \tag{2.24a}
 \end{aligned}$$

$$E_{out} = E_{in} \frac{\sqrt{T_1^{cav} \cdot T_2^{cav}} e^{d\alpha_x} \cdot e^{i\phi}}{1 - \sqrt{R_1^{cav} \cdot R_2^{cav}} e^{2d\alpha_x} \cdot e^{i\phi}}, \tag{2.24b}$$

$$E_{refl} = \frac{E_{in} \sqrt{R_1} e^{i\pi} + E_{in} T_1 \sqrt{R_2} e^{d\alpha_x} \cdot e^{i\phi}}{1 - \sqrt{R_1^{cav} \cdot R_2^{cav}} e^{2d\alpha_x} \cdot e^{i\phi}}, \tag{2.24c}$$

where the factor $e^{i\pi}$ in Eq.(2.24c) explains the phase shift due to the reflection at an optical denser surface. With knowing $I_i = |E_i|^2$, the normalized intensity can also be written as

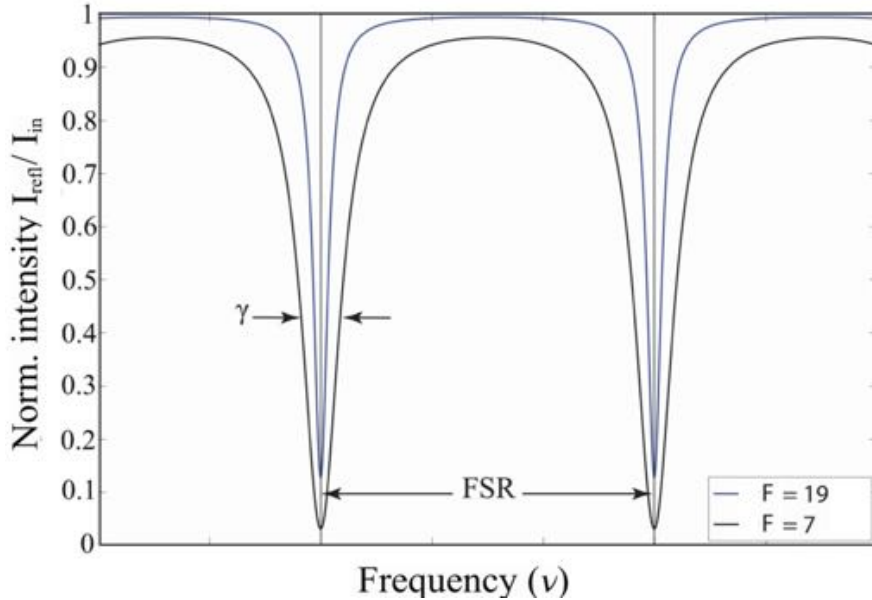


Figure 2.5: The Lorentzian normalized reflected intensity (I_{refl}/I_{in}) peaks for two different finesse number due to different transmitted and reflected value is presented. The free spectral range (FSR) is the distance between two minimum peak position. Full width at half maximum (FWHM) around the one central frequency is also shown with bandwidth γ for different finesse F .

follows [29]:

$$\begin{aligned}\frac{I_{cav}}{I_{in}} &= \frac{T_1}{(1 - \underbrace{\sqrt{R_1 R_2} e^{-2d\alpha}}_a)^2 + 4\sqrt{R_1 R_2} e^{-2d\alpha} \sin^2(\phi/2)} \\ &= \frac{T_1}{(1 - a^2)} \cdot \frac{1}{1 + (2\mathcal{F}/\pi)^2 \sin^2(\phi/2)},\end{aligned}\quad (2.25a)$$

$$\frac{I_{out}}{I_{in}} = \frac{T_1 T_2 e^{-2d\alpha}}{(1 - \sqrt{R_1 R_2} e^{-2d\alpha})^2 + 4\sqrt{R_1 R_2} e^{-2d\alpha} \sin^2(\phi/2)}, \quad (2.25b)$$

$$\frac{I_{refl}}{I_{in}} = \frac{(\sqrt{R_1} - (R_1 + T_1)\sqrt{R_2} e^{-2d\alpha}) + 4(R_1 + T_1)\sqrt{R_1 R_2} e^{-2d\alpha} \sin^2(\phi/2)}{(1 - \sqrt{R_1 R_2} e^{-2d\alpha})^2 + 4\sqrt{R_1 R_2} e^{-2d\alpha} \sin^2(\phi/2)}, \quad (2.25c)$$

In Eq.(2.25a) we introduce the finesse \mathcal{F} which is generally used as a measure for the quality of cavity

$$\mathcal{F} = \frac{\pi\sqrt{|a|}}{1 - |a|}, \quad (2.26)$$

where, $a = \sqrt{R_1 R_2} e^{-2d\alpha}$. Consider the π phase shift in Eq.(2.24c) if both outgoing and reflected fields are equal in amplitude, the result will be zero due to total destructive interference in the reflection port at the critical frequency ν_0 . This case is called resonator critical coupling and described by:

$$\sqrt{R_1} = \sqrt{R_2} e^{-2d\alpha} \quad \text{critical coupling.} \quad (2.27)$$

The two other case are:

$$\sqrt{R_1} > \sqrt{R_2} e^{-2d\alpha} \quad \text{over coupling,} \quad (2.28)$$

$$\sqrt{R_1} < \sqrt{R_2} e^{-2d\alpha} \quad \text{under coupling.} \quad (2.29)$$

Over coupling and under coupling cases lead to reflection and the transmission is not optimum. The maximum output intensity I_{out} is also reached for critical coupling. Regarding Eq.(2.27-2.29) with changing the reflection or optical path one can change the coupling regime.

In case of high frequency, the intensity in reflection port can be modeled with Lorentzian function. The full width at half maximum (FWHM) around the central frequency at normalized reflection intensity I_{refl}/I_{in} is called the resonator bandwidth γ (see Fig.2.5). The spacing in optical frequency between two successive reflected or transmitted optical intensity maxima or minima is called free spectral range (FSR) and it derived from Eq.(2.22)

$$\text{FSR} = \frac{c}{2dn} = \frac{1}{\tau}, \quad (2.30)$$

where τ donates the light round trip time in the resonator. Consequently, the *FSR* can also be written as (see [28] for proof):

$$\text{FSR} = \gamma \cdot \mathcal{F}. \quad (2.31)$$

Another important parameter for characterizing a cavity is the quality factor Q which describes ability of the cavity to store energy. The Q factor of a resonant cavity is given by:

$$Q = \frac{2\pi\nu_0 E}{P}, \quad (2.32)$$

where E is the stored energy in the cavity and $P = -dE/dt$ is the power dissipated in one oscillation period. Also, Q is equal to the ratio of the resonant frequency to the bandwidth of the cavity resonance.

$$Q = \frac{\nu_0}{\gamma} \quad (2.33)$$

A high finesse and Q factor can be achieved with proper coating of end mirrors or with total internal reflection mechanism.

2.3.2 Mode spectrum

The knowledge of mode in WGR can help to describe evanescent field effect of specific mode and to control the narrow-band phase-matching conditions in nonlinear processes such as second-harmonic generation (SHG) or parametric down-conversion (PDC).

The full information on the mode numbers is contained in the far field images of the outcoupled modes, and in the frequency spectrum of the outcoupled light. However, the exact identification of whispering-gallery modes (WGM) can be challenging in practice [30].

By using Maxwell's equations (2.1a, 2.1b, 2.2a, 2.2b), we determine the structure of the fields in a dielectric sphere located in vacuum. To solve this problem, it is convenient to use the spherical coordinate system r, θ, ϕ and solving the Helmholtz equation $\nabla^2 U + k^2 U = 0$ for a dielectric sphere, with appropriate boundary conditions [11]. The Helmholtz equation in spherical coordinate is:

$$\frac{\partial^2 U}{\partial r^2} + \frac{1}{r^2 \sin \theta} \frac{\partial}{\partial \theta} \left(\sin \theta \frac{\partial U}{\partial \theta} \right) + \frac{1}{r^2 \sin^2 \theta} \frac{\partial^2 U}{\partial \phi^2} + k^2 U = 0, \quad (2.34)$$

where U is a scalar function represents the complex amplitude of \vec{E} for any of its three components (E_r, E_θ, E_ϕ) or (H_r, H_θ, H_ϕ) of magnetic field \vec{H} . The electric and magnetic field can be written as:

$$E_r = \left(\frac{\partial^2}{\partial r^2} + k^2 \right) U, \quad H_r = 0, \quad (2.35a)$$

$$E_\theta = \frac{1}{r} \frac{\partial^2 U}{\partial r \partial \theta}, \quad H_\theta = ik \frac{1}{r} \frac{\partial U}{\partial \phi}, \quad (2.35b)$$

$$E_\phi = \frac{1}{r \sin \theta} \frac{\partial^2 U}{\partial r \partial \phi}, \quad H_\phi = ik \frac{1}{r} \frac{\partial U}{\partial \theta}, \quad (2.35c)$$

which $k = k_0(\epsilon\mu)^{1/2}$ is wave number inside the sphere and $k = k_0 = \omega/c$ is wave number outside the sphere [31]. If we assume the potential U in the form:

$$U(r) = R(r)\Theta(\theta)\Phi(\phi), \quad (2.36)$$

then, by substituting this to Eq.(2.35) we have:

$$\Theta(\theta) = P_n^m(\cos \theta), \quad (2.37)$$

$$\Phi(\phi) = \begin{cases} \sin m\phi \\ \cos m\phi \end{cases} \quad (2.38)$$

For a sphere of radius R and refractive index n , the solution is in the form:

$$U_{ml}^i(r, \theta, \phi) \propto \sqrt{r} J_{l+1/2}(nk_0 r) P_m^l(\cos \theta) \exp(\pm im\phi), \quad (2.39)$$

inside the dielectric sphere ($r \leq R$) and

$$U_{ml}^e(r, \theta, \phi) \propto \sqrt{r} H_{l+1/2}^{(1)}(nk_0 r) P_m^l(\cos \theta) \exp(\pm im\phi) \quad (2.40)$$

outside the dielectric sphere ($r > R$). Here J_l is the Bessel function of the first kind of order l , $H_l^{(1)}$ is the Hankel function of the first kind of order l , and P_m^l is the Legendre function. In a way of solving this equation the field \vec{E} and \vec{H} inside the sphere should satisfy the conditions on the boundaries. These conditions can be satisfied after the appropriate choice of a free parameter k_{0a} and arbitrary constants $C_{i,e}$. The continuity condition for the tangential components of the field at the interface between the sphere and vacuum leads us to the characteristic equations determining the acceptable values for k_{0a} and the relation between wave number k and the sphere radius R . Because the characteristic equation contains many roots, they determine an infinite set of the wave vectors (eigenfrequencies) for a given radius of the sphere. In this case, it is necessary to introduce the index q , which indicates the corresponding solution.

For this reason, the eigen modes of a dielectric sphere are described by three indices m , l , q . The greater the root number q , the greater number of zeroes of the function are located inside the sphere. As a result the index q corresponds to the number of nodes of the given mode lying inside the sphere along the radial direction. The number m defines the field nodes along ϕ direction which in general it is quite large for the large radius WGR (m is in range of 10^4 in these experiments), and l is the number of field maxima in polar direction.

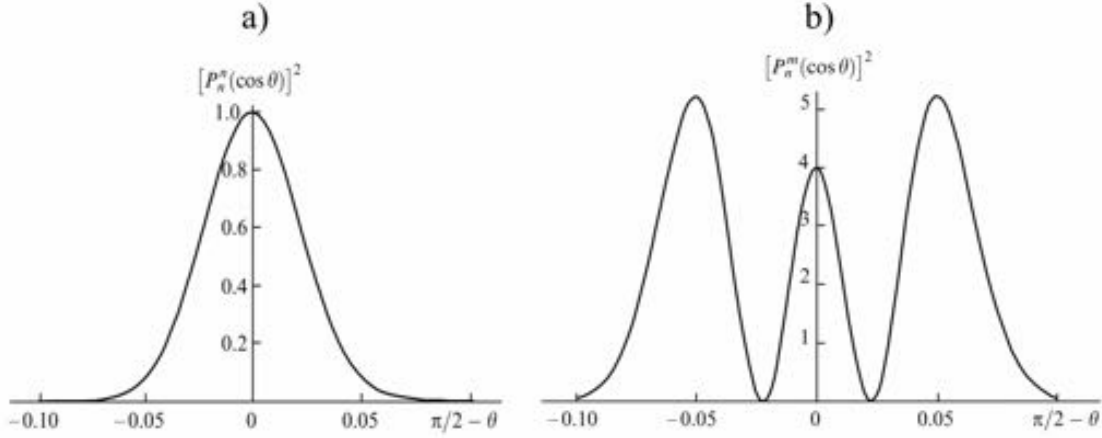


Figure 2.6: The angular dependence of the fields is given by the associated Legendre polynomials $P_l^m(\cos \theta)$. In a) the angular shape of a mode with $m=l$ and $l=1000$ is shown. In b) this angular shape for $m-l=2$ ($p = 2$) and $l=1000$ is depicted [32]

Another number $p = l - |m|$, which is not independent number, defines as angular mode number. The spherical modes are similar to the modes of Gaussian beam [32] with radius of $(2/l)^{1/2}R$. Therefore we have:

$$\frac{P_l^m(\cos \theta)}{P_l^m(0)} \approx \frac{H_{m-l}(\sqrt{n}(\frac{\pi}{2} - \theta))}{H_{m-l}(0)} \exp\left(-l\left(\frac{\pi}{2} - \theta\right)^2/2\right) \quad (2.41)$$

with the Hermitian polynomials $H_{m-l}(\sqrt{l}\theta)$. This equation can help us to find the shape of Gaussian beam for different p value (see Fig.2.6). The mode with high $l = m$ value is very close to equator and referred as fundamental modes when the q number is one. Modes with non-zero p value can exhibit an oscillation in transverse structure.

In this project we are considering the WGR which is looks like a cross section of a sphere (see Fig.2.7.b). For such a resonator, one can connect the mode numbers l, q , and p to the resonant optical frequency $\nu_{l,q,p}$ with using the dispersion relation [30].

$$\begin{aligned} \nu_{l,q,p} = \frac{c}{2\pi n R} \cdot \left[l + \alpha_q \left(\frac{l}{2}\right)^{1/3} + p \left(\sqrt{\frac{R}{r}} - 1\right) - \frac{x \cdot n}{\sqrt{n^2 - 1}} + \frac{1}{2} \sqrt{\frac{R}{r}} \right. \\ \left. + \frac{3\alpha_q^2}{20} \left(\frac{l}{2}\right)^{-1/3} + O(l^{-2/3}) \right] \end{aligned} \quad (2.42)$$

which r is radius of disk curvature (small radius), parameter x is 1 or $1/n^2$ depending on polarization and n is the refractive index of disk resonator. The q -th root of the Airy function α_q , 0 can be approximated as $\alpha_q = [3/2(q1/4)]^{2/3}$. This equation determines the resonance frequency of each mode and it can be useful to extract the temperature dependency of frequency shifts of a mode

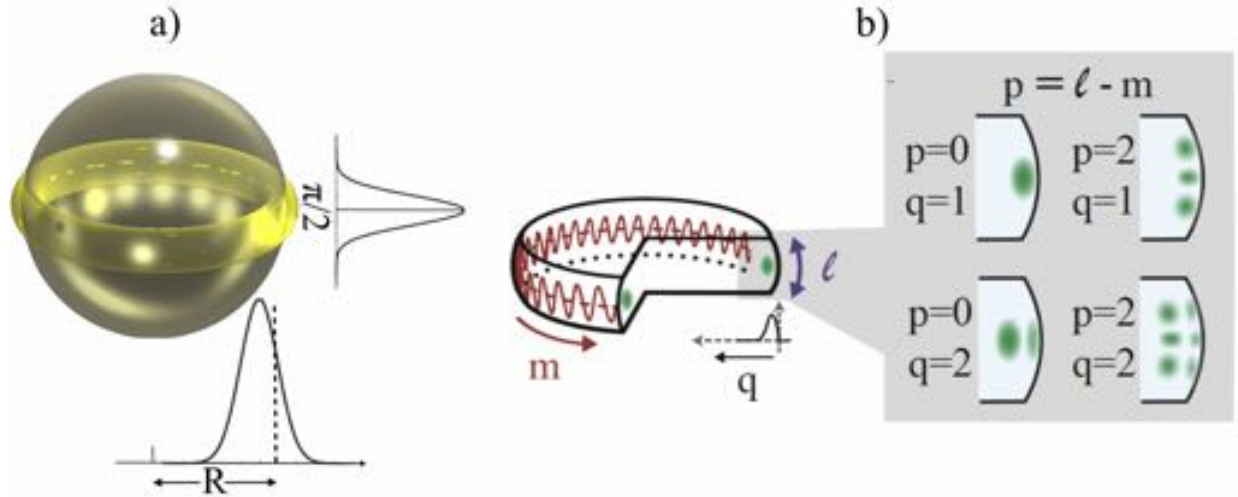


Figure 2.7: a) Whispering-gallery mode in a microsphere resonator with radius R . The intensity of the electromagnetic field decays exponentially out of the resonator b) The radial q , azimuthal m and polar l number of the mode is associated with spatial position of the mode in spherical reference [30]. The angular mode number $p=l-m$ gives the number of maxima in polar direction.

TE and TM Modes

The mode inside the WGR made of dielectric material can classify in three groups regarding the polarization and boundary condition. In this classification the light that is polarized parallel to the optical axis is called transverse electric (TE) modes and has no electric field in the direction of propagation, the light that is polarized perpendicular to the optical axis is called transverse magnetic (TM) modes and has no magnetic field in the direction of propagation and the light which is linearly with angle to optical axis or circularly polarized is called TEM modes. If the WGR made of a birefringent crystal, each of these polarized modes can have different refractive indices (see section 2.1.2) and consequently different frequencies.

2.3.3 Evanescent field coupling

In general, methods of coupling the light into the WGR are divided into three categories: free wave coupling, fluorescent coupling and evanescent coupling.

In free wave coupling, by illuminating the resonator from the outside, one can excite whispering gallery modes inside the resonator. Similarly, the excited WGMs can also leak out of the resonator into the free space. This form of coupling is extremely inefficient even for ultra-high-Q resonators.

Florescent coupling is based on doped resonators with a fluorescent substance (e.g. quantum dots), which emits a broad spectrum of light when excited at a short wavelength. By illuminate the doped whispering gallery resonator, the fluorescent substance in the resonator

starts emitting a broad spectrum of longer wavelength light, which then gets trapped inside the resonator.

In evanescent field coupling the light can be coupled in or out of WGR by using fiber tapers, side-polished fiber coupling, or prisms. This method has a high coupling efficiency and therefore it is the method which we used in this experiment. In practice, efficient coupling with this method needs a fine alignment. Evanescent field coupling occurs when a structure possessing an optical evanescent field has been brought in the vicinity of the resonator, so that the evanescent fields of the resonator and the coupler overlap significantly. As an example, prism evanescent field coupling is illustrated in Fig.(2.8). The following description is based on [33, 23, 34]. Due to the total internal reflection inside the resonator, in high-Q WGR the field drops outside the resonator approximately as $\exp(-\gamma r)$ where:

$$\gamma^2 \approx k^2(n_s^2 - 1) \quad \text{and,} \quad k = (2\pi/\lambda)\sqrt{n_s^2 - 1}$$

for resonator surrounded by air. Here n_s is the resonator refractive index. For a given wavelength λ of the coupling beam, one can calculate the angle of incidence for n_s refractive index of resonator and n_p refractive index of prism with Snell's law:

$$\sin \theta_0 = \frac{n_s}{n_p}. \quad (2.43)$$

With assumption that the wave which is propagated inside the prism and resonator is a plane wave and with geometry of Fig.(2.8), one can derive $kn_p \sin \theta_0 = kn_s$. This condition can be satisfied if the WGR exhibit equal or lower refractive index than the prism. Overlapping the resonator and the prism evanescent field produce a coupling between them which is calculated as follow.

The field of resonator E_R for the chosen j-th mode can be driven from Eq.(2.39, 2.40) and conveniently represented in the form:

$$E_R = e_R^j b_j E^{-i\omega_j t} + c.c., \quad (2.44)$$

where R is the resonator radius, b_j is the slow amplitude, m_j is the characteristic frequency and e_R^j describes the spatial distribution field of the mode in an isolated dielectric sphere. The plane wave which is incident on the inner surface of the prism at an angle greater than the angle of total internal reflection (θ_0) has a field of E_p where:

$$E_p = \int e_p^\beta a_\beta(t) e^{-i\omega_\beta t} d\beta + c.c. \quad (2.45)$$

The $a_B(t)$ are the slowly varying spatial amplitudes. By substituting Eq.(2.44) and (2.45) into the Maxwell's equations and performing spatial integration and averaging over time, we can obtain the overlap integrals. The coupling is determined by the overlap integral of the evanescent fields of prism and WGM. The normalized reflected intensity, which is the transmittance T , is described by:

$$T = \left[\frac{1 - A.c e^{-2kd}}{1 + c e^{-2kd}} \right]^2, \quad (2.46)$$

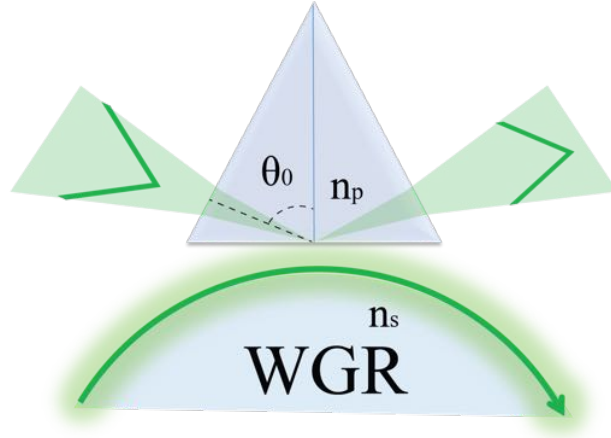


Figure 2.8: Evanescent field coupling with a diamond prism. θ_0 is the coupling angle and determined by the total internal reflection condition.

The prefactor A describes the modal overlap integral between the incident field in the prism and the propagating mode in the resonator which is normally $0 \leq A \leq 1$. c is the ratio between the intrinsic losses and the highest possible coupling losses and d is the gap between the resonator and the prism.

The Q -factor in WGMRs can be described as:

$$\frac{1}{Q} = \frac{1}{Q_0} + \frac{1}{Q_c}, \quad (2.47)$$

where Q_0 is the intrinsic quality factor:

$$Q_0 = \frac{2\pi n_s}{\alpha \lambda}, \quad (2.48)$$

and Q_c is the loading quality factor parameter for prism coupling:

$$Q_c \approx \frac{\sqrt{2}\pi^{5/2} n_s^{1/2} (n_s^2 - 1)}{(n_c^2 - n_s^2)^{1/2}} \left(\frac{R}{\lambda}\right)^{3/2} \exp(2\gamma d). \quad (2.49)$$

The α is linear attenuation in the resonator caused by scattering, absorption, and radiation. indices s , c are related to the resonator and the coupler (prism), respectively. The other parameters are determined previously. Loading quality factor depends on coupling prism distance. The total Q versus distance is shown in Fig.(2.9) for different wavelength.

2.3.4 Parametric down conversion

A material with second-order susceptibility $\chi^{(2)}$ can connects two electrical fields to generate a third one. commonly, the process, where two sub-harmonics fields are used to generate an harmonic field, is called sum frequency generation. In the special case that the two sub-harmonics comprise the same oscillation frequency, this process is called second harmonic

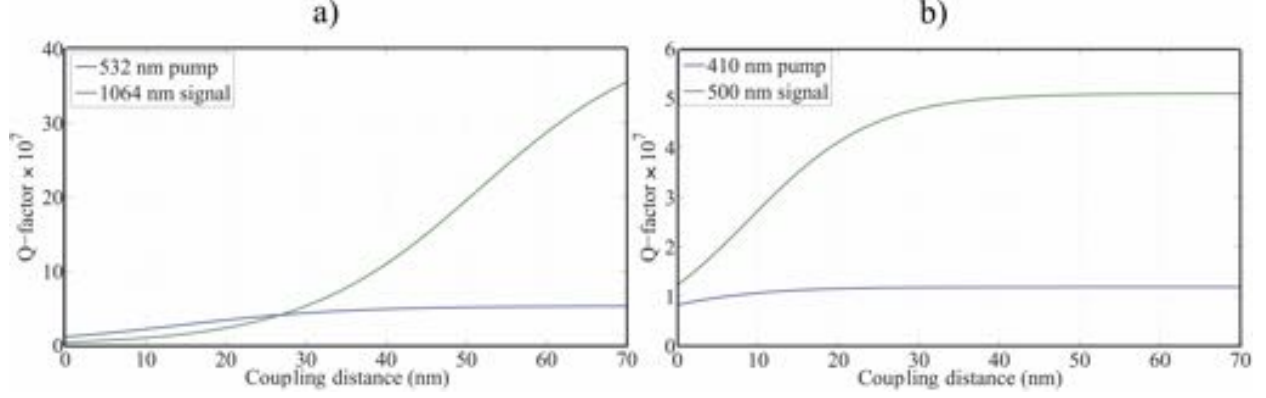


Figure 2.9: The theoretical Q-factor value versus the distance between the coupling prism and the resonator. The intrinsic quality factor Q_0 is determined when the coupling prism is far from the resonator. a) The Q-factor in resonator with $R=1.9$ mm and the pump and signal wavelength at 532 nm and 1064 nm, respectively. b) The Q-factor in resonator with $R=1.08$ mm, and pump=410 nm and signal=500 nm.

generation. In reverse, if one harmonic field is used to generate two sub-harmonics, the process is called parametric down conversion (PDC). In practice for PDC, pump photons (p) incident on a nonlinear crystal can be converted into two photons, called the signal (s) and idler (i). This process is important in quantum optics, used especially to produce entangled photon pairs, and also constitutes an excellent method to produce a source of single photons [35].

According to energy conservation rule, the sum of the energies of signal and idler will always match the energy of the pump (p). In Ref. [36] the coupled wave equations for the parametric amplification process in a linear resonator with length L have been defined as:

$$\begin{aligned} \left(\frac{\partial}{\partial t} + \Gamma_p \right) \alpha_p &= i\sigma \alpha_s \alpha_i \exp(i\Delta\omega t), \\ \left(\frac{\partial}{\partial t} + \Gamma_s \right) \alpha_s &= i\sigma^* \alpha_i \alpha_p^* \exp(i\Delta\omega t), \\ \left(\frac{\partial}{\partial t} + \Gamma_i \right) \alpha_i &= i\sigma^* \alpha_s \alpha_p^* \exp(i\Delta\omega t), \end{aligned} \quad (2.50)$$

with the conversion efficiency (overlap integral) of:

$$\sigma = \frac{1}{2L} \int_0^{2L} x^{(2)} \exp(i\Delta k y) dy. \quad (2.51)$$

Here, $\alpha_{p,s,i}$ are the slow varying amplitudes and $\Gamma_{p,s,i}$ are the corresponding loss coefficient. The propagation direction is chosen to be in y -direction and the mismatch in the wave vectors Δk and the energy $\Delta\omega$ is given by:

$$\Delta k = k_p - k_s - k_i, \quad \Delta\omega = \omega_p - \omega_s - \omega_i. \quad (2.52)$$

There are two main conditions, which have to be fulfilled in an efficient phase matching. First, the energy between the modes must be conserved. This implies, that the energy mismatch $\Delta\omega$ has to be far smaller than the loss coefficients Γ_p and $\Gamma_{s,i}$. Second, the conversion efficiency (Eq.2.51) should be maximal. Therefore, either Δk should be minimal. In birefringent materials the PDC process can also depends on polarization. Whenever the signal and idler have the same polarization (ordinary or extraordinary) and oppose to the pump polarization is called type I parametric down conversion and when signal and idler have a different polarization is called PDC type II.

In order to describe the field in WGRs, one can use the spherical geometry. As a result, the angular part of a whispering-gallery mode (WGM) is described by spherical harmonics Y_m^l , and the radial part is described by spherical Bessel functions $j(k_q r)$. In this case the linear conversion efficiency (Eq.2.51) becomes:

$$\sigma = x^{(2)} \int j_p^*(k_p r) j_s(k_q r) j_i(k_q r) dr \int \int Y_{m_p}^{*l_p} Y_{m_s}^{l_s} Y_{m_i}^{l_i} \sin \theta d\theta d\phi, \quad (2.53)$$

where the radial and the angular part of the general wave equation has been separated in Eq.(2.53).

Now with writing interaction Hamiltonian, one can derive the equation of motions which are related to Langevin forces and these forces are also related to the pump power [37]. With calculating this value in the critical coupling condition, one can obtain the PDC power threshold for the different wavelength λ [38].

$$P_{th} = \frac{c}{\lambda_p Q_p} \left(\frac{n^3}{16\pi\sigma x^{(2)} Q_s} \right)^2, \quad (2.54)$$

where, Q_p , Q_s are the quality factor of pump and signal respectively, n is the refractive index of WGR and σ is the overlap integral. This equation can helps us to estimate the minimum value of pump power for PDC generation.

2.3.5 Temperature tuning of the mode spectrum

Any small change of the optical length of resonator causes the resonance frequency shift. Thermal changes can affect the refractive index (thermal refractivity) and size of the resonator (thermal expansion) [39]. Former is calculated by Sellmeier equation 2.17 and latter calculate with Eq.(2.19). In an anisotropic crystal (e.g. lithium niobate) these effects can provide different resonance shifts regarding the polarization and number of the modes (see section 2.2).

To find out the relation between frequency shifts with temperature one can starts with WGM dispersion equations which have been discussed as a complete form in [40] and the truncated form, which retains only positive powers of the orbital momentum L in [24]:

$$\frac{f n}{2\pi c} \approx \frac{1}{R} [L + \alpha_q (L/2)^{1/3}], \quad (2.55)$$

where f is the WGM frequency, R is the resonator radius and n is the refractive index for given polarization and wavelength. Here, n and R are functions of temperature T . By differentiating Eq.(2.55) with respect to T , we have:

$$\frac{1}{f} \frac{df}{dT} + \frac{1}{n} \frac{dn}{dT} + \frac{1}{R} \frac{dR}{dT} = 0. \quad (2.56)$$

The second term of Eq.(2.56) are equal to the thermorefractivity $\alpha_n^{(o)}$ and $\alpha_n^{(e)}$ for ordinary and extraordinary mode, respectively. The third term is equal to thermal expansion coefficients and have a same value for both polarization modes:

$$\frac{d}{dT} f_{o,e} \approx \frac{c}{\lambda} \alpha_l^{(o)}, \quad (2.57)$$

which c and λ are light speed and beam wavelength in vacuum, respectively. The frequency difference between the modes depends only on the differential thermorefractivity while the thermal expansion is the same for both modes. Consequently, the temperature variations in WGR is zero if the frequency shifts of two modes with different polarization (TE and TM) regarding to each other is zero.

$$\frac{d}{dT} \Delta f \approx \frac{c}{\lambda} (\alpha_n^{(o)} - \alpha_n^{(e)}). \quad (2.58)$$

When the temperature changes, the frequency shifts is different for each mode regarding to its numbers. By using Eq.(2.42), we can find the the frequency shifts via the temperature (see Fig.2.10).

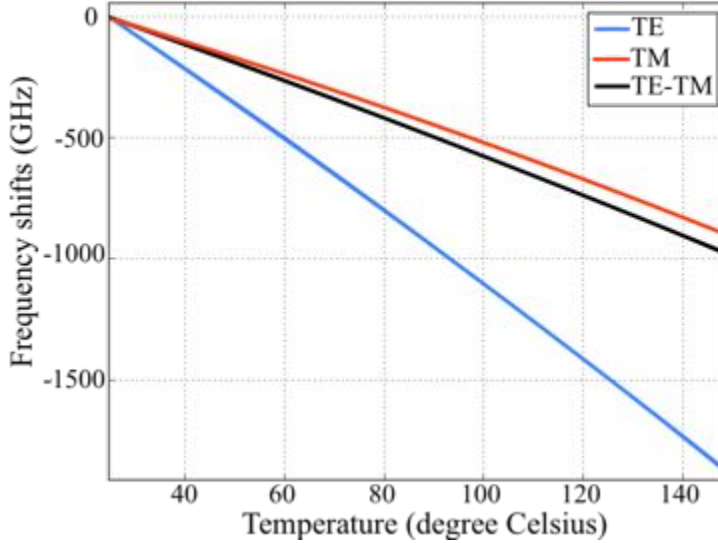


Figure 2.10: The numerical simulation of frequency shifts via the temperature of lithium niobate WGR with $R = 1.08$ mm. All modes have a red shifting with the temperature increase. These shifts is shown for TE, TM and the difference between them at $\lambda = 820$ nm.

2.3.6 Pressure tuning of the mode spectrum

Applying pressure on a WGR can change the geometry or the material property of it and as a result change the resonance frequency of the WGR. In order to obtain the pressure effect in WGR, we assume the hollow spherical resonator with outer diameter R and inner diameter b as shown in Fig.(2.12) in hydrostatic pressure surrounding the sphere. We should note that in this experiment we have an asymmetric pressure on a disc shape resonator. As a result, this theory cannot fit to the experimental data completely but here the mode behavior (not exact shift) via the pressure is considered.

As stated in Eq.(2.22) the approximate resonance condition for a WGR is:

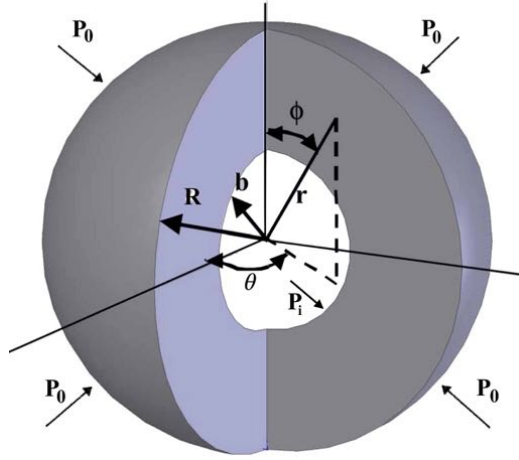


Figure 2.11: A hollow spherical WGR under hydrostatic external pressure P_0 [41].

$$m\lambda_0 = 2\pi Rn \quad (2.59)$$

with substituting $2\pi R$ with d . A fractional change in both the index of refraction and the radius will induce a shift in the WGM [41]:

$$\frac{d\lambda}{\lambda} = \frac{dn}{n} + \frac{dR}{R} \quad (2.60)$$

In the following we will derive the analytic expression for both strain (da/a) and stress (dn/n) effect due to hydrostatic pressure. The change of refractive index with the applied mechanical stress is given by the Neumann-Maxwell equation:

$$\begin{aligned} n_r &= n_{0r} + C_1\sigma_{rr} + C_2(\sigma_{\theta\theta} + \sigma_{\phi\phi}) \\ n_\theta &= n_{0\theta} + C_1\sigma_{\theta\theta} + C_2(\sigma_{rr} + \sigma_{\phi\phi}) \\ n_\phi &= n_{0\phi} + C_1\sigma_{\phi\phi} + C_2(\sigma_{\theta\theta} + \sigma_{rr}) \end{aligned} \quad (2.61)$$

where σ_{rr} , $\sigma_{\theta\theta}$, $\sigma_{\phi\phi}$ are distributions of the principal stresses in the radial r , tangential θ , and polar ϕ , directions, respectively. The σ is a function of b , a , p_0 and p_i . The n_r , n_θ , n_ϕ are

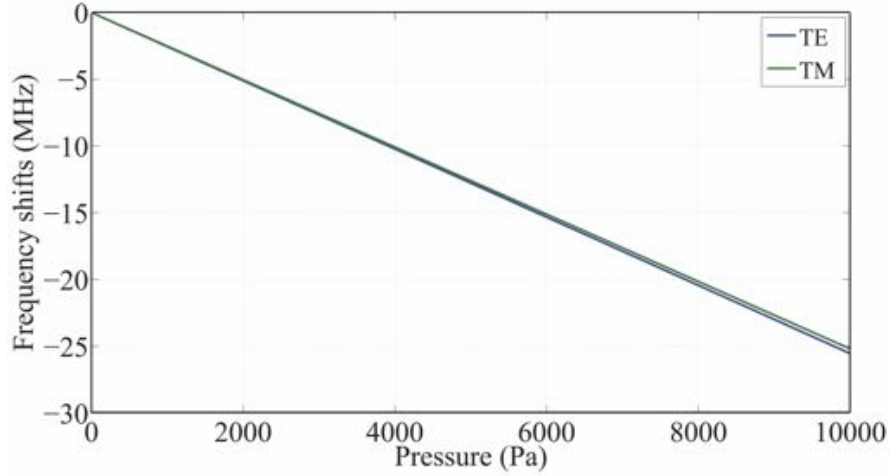


Figure 2.12: The frequency shifts in spherical WGR made of lithium niobate under hydrostatic pressure at 532 nm wavelength (see Eq. 2.64).

the refractive indices in the direction of the three principle stresses and $n_{0r}, n_{0\theta}, n_{0\phi}$ are those values for the unstressed material. C_1 and C_2 are the elasto-optical constants as described in section 2.2.3 for lithium niobate. Now the fractional change in the refractive index due to mechanical stress is:

$$\frac{dn}{n} = \frac{n_r - n_{0r}}{n_{0r}} = \frac{n_\theta - n_{0\theta}}{n_{0\theta}} = \frac{n_r - n_{0\phi}}{n_{0\phi}}. \quad (2.62)$$

With substituting Eq.(2.61) into Eq.(2.62) we can find the refractive index variation due to the pressures p_0 and p_i .

The radial displacement u of any point r inside sphere is obtained as:

$$u(r) = \frac{r}{2G} \left[P_i \frac{\frac{1}{2} \left(\frac{R}{r}\right)^3 + \frac{1-2\nu}{1+\nu}}{\left(\frac{R}{b}\right)^3 - 1} - P_0 \frac{\frac{1}{2} \left(\frac{b}{r}\right)^3 + \frac{1-2\nu}{1+\nu}}{1 - \left(\frac{b}{R}\right)^3} \right] \quad (2.63)$$

which G and ν are the shear modulus and the Poisson ratio of the sphere material, respectively. These constant value are obtained from elastic compliance tensor. The external pressure P_0 and inner pressure, P_i are also appear in Eq.(2.63) and distributions of the principal stresses. The displacement for WGR with radius R is $u(R)/R = dR/R$. Summation of the refractive index and the radius changes according to Eq.(2.60) gives us the wavelength variation for a hollow sphere resonator. In special case, for solid resonator $b = 0$ and neglect inner pressure P_i :

$$\frac{\Delta\lambda}{\lambda} = -\frac{1}{2G} P_0 \frac{1-2\nu}{1+\nu} - \frac{1}{n} P_0 (2C_2 + C_1). \quad (2.64)$$

The graph for frequency shifts in lithium niobate is shown in Fig.(2.12). The same method of pressure effect has been explained in Ref. [25] as a high resolution force sensor.

2.3.7 Frequency shifts induced by a dielectric coupler

The light inside the whispering-gallery resonator (WGR) is confined with total internal reflection and provide the evanescent field around the resonator. By inserting a material like a dielectric into this field one can change the property of the filed. In order to calculate this effect we model the resonator as a cylinder shape as shown in Fig.(2.13). The incident electric filed E_i is scattered in all direction of resonator's plane (evanescent field) which has been shown with E_s . Due to presence of dielectric material the scattered field from the resonator is reflected by dielectric and giving rise to the field E_{sr} . The total field incident upon the resonator is that formed from the superposition of the incident field and the reflected scattered field ($E_{eff} = E_i + E_{sr}$).

The mode shifts can be driven in the resonator via position of the dielectric substrate [42],

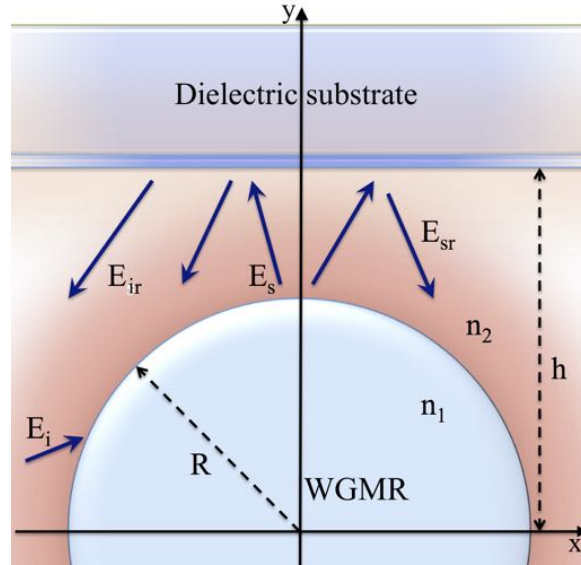


Figure 2.13: The geometry of evanescent field shifts problem. The incident field E_i is scattered by WGR and reflected from the prism surface giving rise to a field E_{ir} which is neglectable. The scattered field E_s is reflected due to dielectric surface and produce the E_{sr} field. The effective coupling field is a superposition of E_s and E_{sr} [42].

$$\frac{\Delta\omega_k}{\gamma_k} = -\eta_{k,0}^\nu \text{Im}[K_{kk}^\nu]. \quad (2.65)$$

where $\Delta\omega_k$ is the resonance frequency shifts, γ_k and $\eta_{k,0}^\nu$ are the bandwidth and scattering coefficient, respectively. K_{kk}^ν is the complex self-coupling coefficient.

Equation 2.65 describes the resonance frequency change from introduction of any perturbing structure e.g. prism or particle. Here, we are trying to derive the self-coupling coefficient for a disc resonator, perturbed by a planar interface based upon a Mie scattering and Fresnel-type reflection methodology. Reflection of each plane wave component at the

prism surface can be described using the Fresnel reflection coefficient, such that we can write:

$$E_{sr,m}^\nu(r) = \sum K_{m,m'}^\nu E_{m'}^{\nu,(3)}(r) \quad (2.66)$$

The coupling coefficients follows by evaluation of the integrals

$$K_{m,m'}^\nu = \frac{\int_0^{2\pi} [E_{m'}^{\nu,(3)}(r)]^\dagger \cdot E_{sr,m}^\nu(r) d\phi}{\int_0^{2\pi} |E_{m'}^{\nu,(3)}(r)|^2 d\phi} \quad (2.67)$$

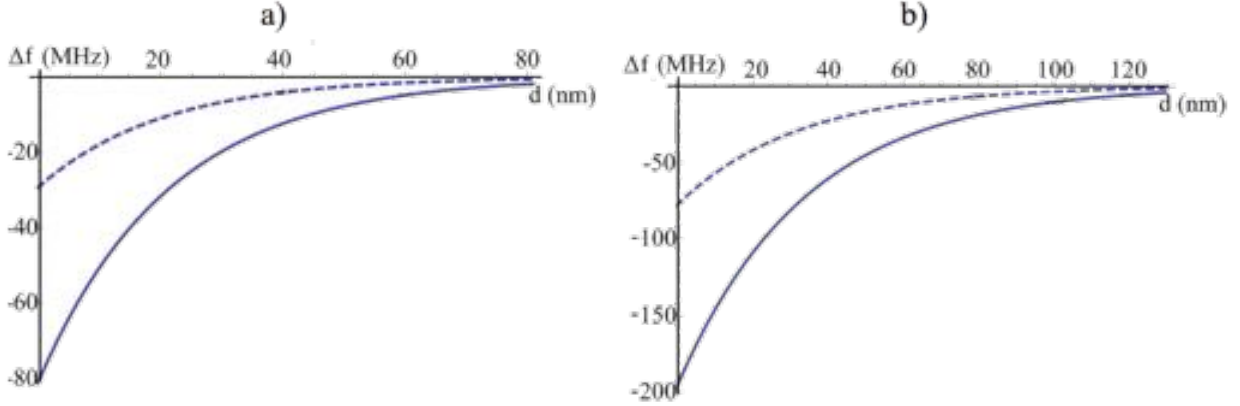


Figure 2.14: WGMR resonance shifts via movable ZnO dielectric substrate for different size of resonators: a) $R=2.5$ mm and b) $R=1.6$ mm. Solid and dash lines depict calculations for TM and TE modes respectively.

For different polarization the K_{kk}^ν in Eq.(2.65) is changed to:

$$K_{m,m'}^{TE} = \frac{i^{(m'-m)}}{\pi} \int_{\Gamma_+} r_s(\beta) \exp[i(m+m')\beta] \exp[2in_2kh \sin \beta] d\beta \quad (2.68a)$$

$$K_{m,m'}^{TM} = \frac{i^{(m'-m)}}{\pi} \int_{\Gamma_+} r_p(\beta) \exp[i(m+m')\beta] \exp[2in_2kh \sin \beta] d\beta \quad (2.68b)$$

where r_s and r_p denote the reflection coefficient for s and p polarized waves, respectively. The complex propagating angle β is an element of Γ_\pm where Γ_\pm are integration contours in the complex plane. The imaginary and the real part of β can gives us the frequency shifts and the bandwidth of a mode, respectively. With substituting Eq.(2.68) in Eq.(2.65) one can derive the mode shifts equation:

$$\Delta f_m^\nu = -\frac{m\pi c}{2\pi n_2^2 R^2 \pi^2 k N_\nu} [1 - \mu^{-2}]^{1/2} \left[\frac{\rho\mu + \sqrt{\rho^2\mu^2 + 1}}{\mu + \sqrt{\mu^2 - 1}} \right]^{2m} \frac{\exp[-2m\sqrt{1 - \rho^{-2}\mu^{-2}}]}{\exp[-2m\sqrt{1 - \mu^{-2}}]} \times \int_0^\infty \frac{r_\nu(iv)}{\sqrt{1+u^2}} \exp \left[-\frac{m}{\rho^2\mu^2} \sqrt{1 - \rho^{-2}\mu^{-2}} (v - v_{max})^2 \right] dv, \quad (2.69)$$

where $p = m + m'$, $q = 2n_2kh$, $u = \sinh \gamma$, $v = -\sinh \gamma$, $v_{max} = [(p^2/q^2) - 1]^{1/2}$ and $\mu = m/n_2kR$. We also have defined $p/q = \mu(R/h) = \mu\rho$. The variable N_ν for TE and TM

mode states as:

$$N_{TE} = \left(\frac{n_1}{n_2}\right)^2 - 1 \quad (2.70)$$

$$N_{TM} = N_{TE} \frac{\mu^2}{(n_1/n_2)^2 - 1} \quad (2.71)$$

In Fig.(2.14) the solution of this equation via variable distance d is plotted.

Chapter 3

Experimental setup

In this chapter the experimental setup is described. In the first section a method of fabrication of WGMR is explained. The second section introduces the components and different parts of setup. In the third section we calibrate the fine positioner which we used in the experiment. In the last section we will demonstrate a new design of WGMR setup which is portable and more stable.

3.1 Fabrication of whispering-gallery resonator

We fabricate the WGRs from commercially available lithium niobate (LiNbO_3) wafer with 5.8% MgO-doped. We use hollow core brass drill which is mounted on a turning machine and diamond slurry with $30\ \mu\text{m}$ particle to cut out a disc-shape part of the wafer. Then the disc is glued on a brass rod with high-temperature epoxy. The rod has 50 mm height and 13 mm diameter which is tapered towards the tip (see Fig.3.1-a). For the curved rim cut we use a diamond cutter which is controlled by a fine positioner stage close to the rotating disc (see Fig.3.1.b).

To achieve a high Q-factor resonator we polish the resonator's surface while the WGR is turning. The optical tissues impregnated with diamond slurry with different size of diamond particles from $9\ \mu\text{m}$ to $0.1\ \mu\text{m}$ are used for fine polishing. This polishing is done step by step from greater diamond particles to smaller ones. The tissue used for cleaning the disc should be changed in each step to prevent any scratches caused by residual particles on the disc. We use ethanol and isopropanol for cleaning.

To measure the fraction of the radius of curvature of the disc, we use the Newton rings interference patterns. In this technique, a thin transparent plate e.g. glass is placed on top of the resonator in a way that it touches the resonator's rim. The fringes can be observed with a microscope in an elliptic shape which semi-major axes a and semi-minor axes b of ellipsoid are related to radius of the resonator R and curvature r , respectively.

$$a = \sqrt{m\lambda R} \tag{3.1}$$

$$b = \sqrt{m\lambda r} \tag{3.2}$$

The light wavelength is λ and the number of dark fringes is m .

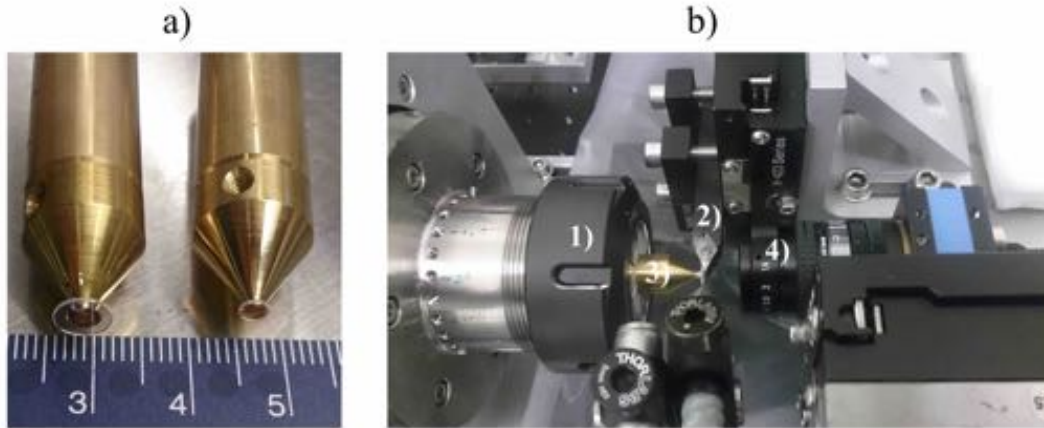


Figure 3.1: a) The rods with different sizes of resonators. The rod consists of two parts which can screw into each other and change the height of resonator in experimental setup. A hole drilled on the top to place a thermistor inside. b) Different parts of turning machine setup: 1) turning machine, 2) diamond cutter, 3) rod and 4) camera.

3.2 Experimental scheme

In this experiment we are trying to tune the resonance frequency of WGR with movable dielectric substrate. We use three different tunable laser diodes with three different resonators. The basic setup for all the measurements is depicted in Fig.(3.2). We use an aluminum chamber to isolate the resonator from temperature fluctuations in the laboratory. Inside the chamber, there are two piezoelectric called Attocube positioner located at two sides of the resonator.

The first piezoelectrics (Attocube) holds the prism coupler and the second piezo a dielectric material which is a glass coated by a layer of zinc oxide with 100 nm thickness or x-cut lithium niobate in these experiment. The surface roughness of ZnO is measured with an atomic force microscope (AFM) (shown in Fig.3.3).

The Attocubes can adjust the distance between the prism and the resonator or the dielectric and the resonator. Two translation mounts (Thorlabs XYZ Translation Mount) hold the lenses with 8 mm focal length close to the resonator. The lens before the prism is called the incoupling lens and it focuses the light into the prism. The lens after the prism which collimates the light again is called outcoupling lens. The polarization of the linear polarized light of the laser can be controlled by a half-wave plate HWP. Together with the polarizing beam splitter PBS we can vary the power ratio of the transmitted (p-polarized) and the reflected (s-polarized) light. The reflected light is coupled to a Fabry-Perot interferometer (Toptica-DL100) with a free spectral range FSR of 1 GHz. The Fabry-Perot signal is monitored by a "Lecroy-wavejet 334" oscilloscope and is used as a frequency reference.

The transmitted light will again pass through a HWP and a PBS. Both the reflected and the transmitted light from PBS should couple to the resonator but due to the different refractive indices for different polarization in lithium niobate (see section 2.2) the outcoupling

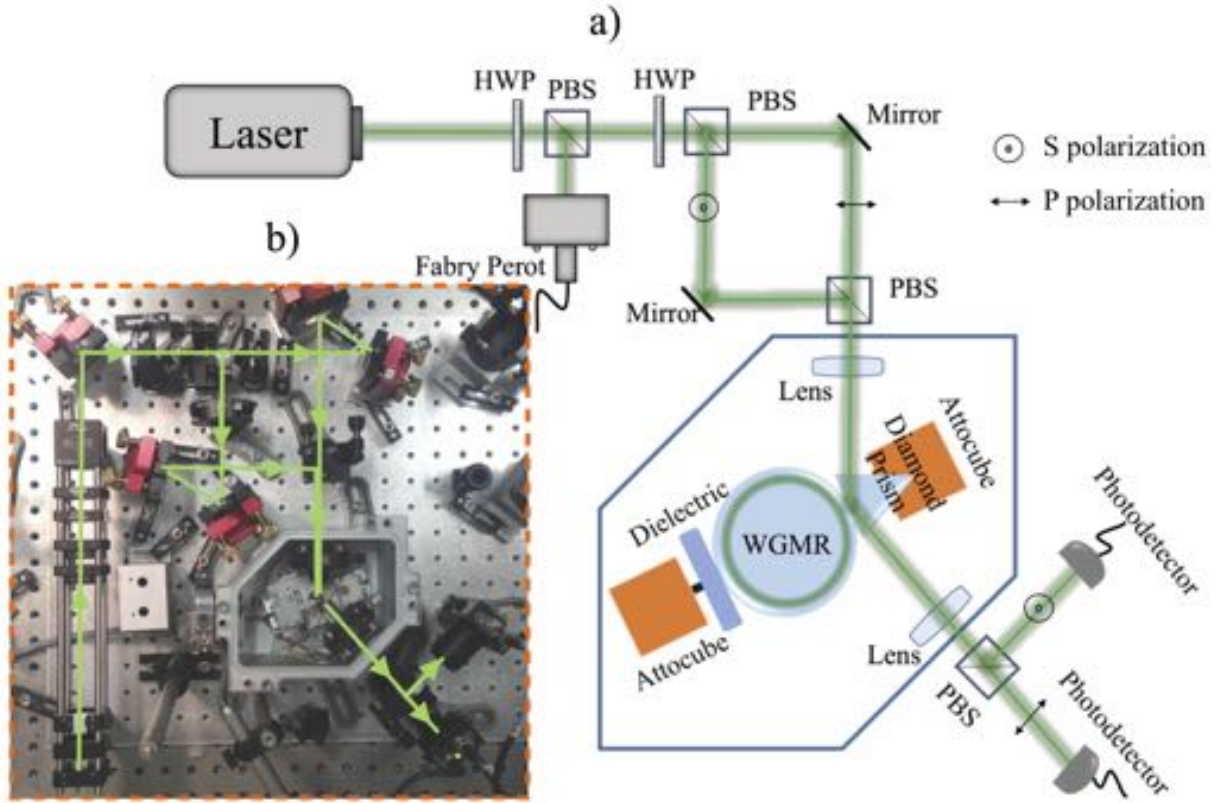


Figure 3.2: a) Scheme of the experimental setup. The polarization of incident light is controlled by half wave plate polarizer HWP. Both p -polarization and s -polarization light are coupled in and out of z -cut WGMR using the diamond prism. The p -polarized and s -polarized light generate TM and TE modes in z -cut WGR, respectively. The outcoupled light is splitted in different polarization with a polarized beam splitter PBS and detected separately. b) A photo of the setup.

angle can be different. These angles are achieved from Eq.(2.43). To compensate this deviation and guide both TE and TM light into the outcoupling lens, we set two beam paths with different polarization and translation mirror mounts. After coupling the light into the resonator, the outgoing light is splitted with the PBS and collected by two photo diodes.

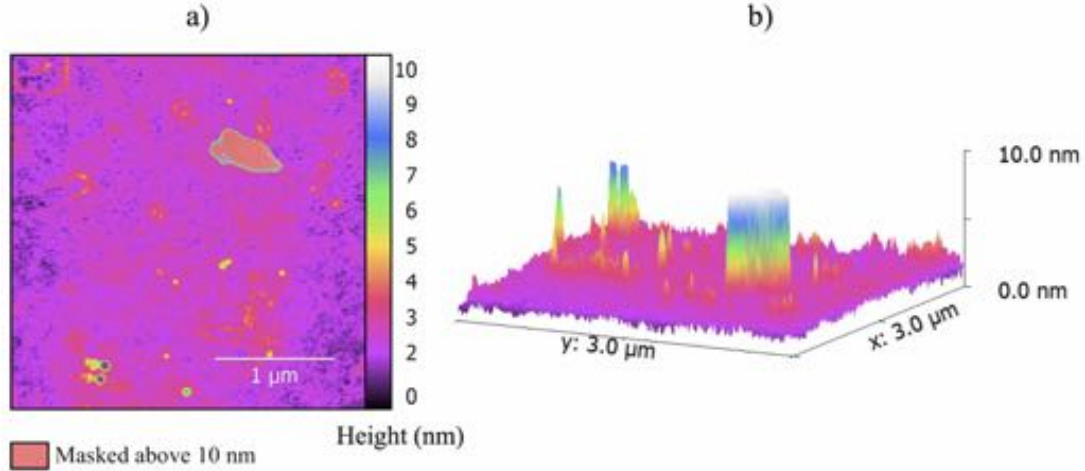


Figure 3.3: Surface roughness measurement of ZnO with atomic force microscopy AFM. The vertical distance resolution of this measurement is 0.1 nm. a) The areas with more than 10 nm height difference are masked. These areas can be some dust particles on the surface of ZnO plate. b) The 3D picture shows 4 peaks with more than 5 nm height.

Light coupling to the resonator

Light coupling to the resonator is done in several steps. The frequency is swept a few GHz by applying a voltage to the piezo mirror (PZT) in the laser. Next, we put the coupling prism in contact with resonator and focus the light on the contacting point. A part of light is reflected from the inner surface of prism and the other part travels through the resonator and coupled out with the prism. Due to different beam paths of the directly reflected light and the light coming from the resonator, form fringe patterns in the far field. We put an outcoupling lens to collimate the light and send it to a detector.

The efficiency of WGR coupling depends on the distance between the prism and the resonator (coupling distance). The distance which has a maximum coupling contrast called critical coupling point. In order to find this point, we put the prism in the contacting position with WGR and move the prism back stepwise for a few nanometers until the modes have maximum coupling contrast (maximum depth).

Optical properties of the resonator

One can characterize the optical properties of the resonator e.g, bandwidth and FSR, by measuring the transmission spectrum. These properties are shown for a R=1.6 mm resonator in Fig.3.4 for TE and TM polarization. The bandwidth is related to the distance between resonator and the prism. We measure the bandwidth close to the critical coupling distance. the amount of bandwidth and FSR allow us to find the fineness or Q-factor (see section 2.3.1)

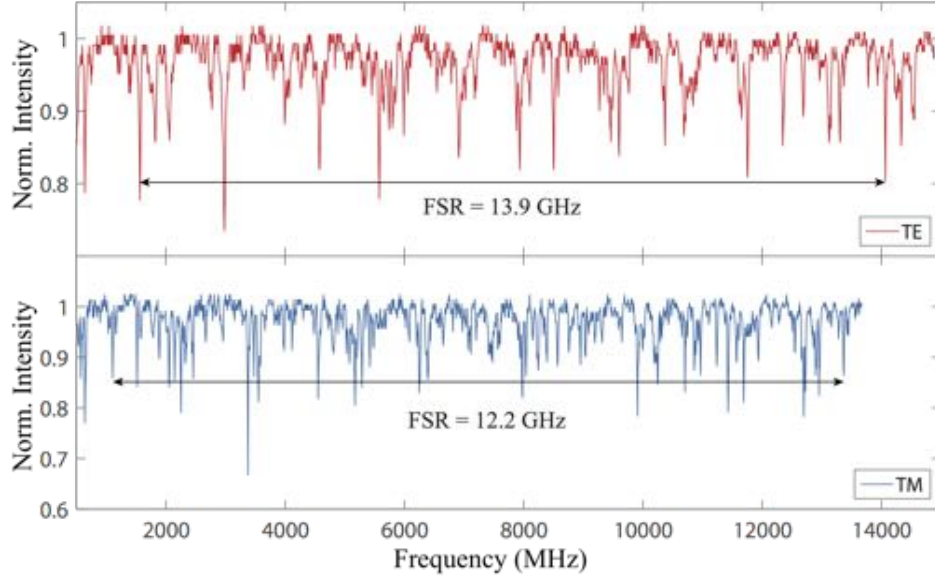


Figure 3.4: FSR range of TE and TM modes for a lithium niobate WGR with $R = 1.6$ mm and $r = 0.16$ mm from the newton ring measurement.

3.3 Calibration of the Attocube positioner

A quantitative description of frequency shifts versus distance requires a calibration of positioner devices. To obtain the absolute distance or displacement in a range of nanometer, we should calibrate the positioner components.

Attocube positioner is a piezoelectric (see [43] for more detail) which can be controlled by a voltage source (attocube controller) and moves stepwise or continuously. A typical way to measure the displacement with high accuracy is to use Michelson interferometer setup as shown in Fig.3.5. In this setup, a movable mirror on the positioner moves towards the PBS stepwise to change the beam path in one arm. The intensity of the interfered light will change due to constructive and destructive interference and is captured by a photo detector. To determine the relation between displacement x of the Attocube and the intensity I , we fit a sinusoidal function to the experimental data (See Fig.3.5).

$$I = A + B.\sin\left(\frac{4\pi x}{\lambda}\right) \quad (3.3)$$

$$x(V) = aV^2 + bV + c \quad (3.4)$$

$$(3.5)$$

The relation between the applied voltage and the Attocube displacement is:

$$x(V) = \frac{\lambda}{4\pi}(-0.008V^2 + 1.188V), \quad (3.6)$$

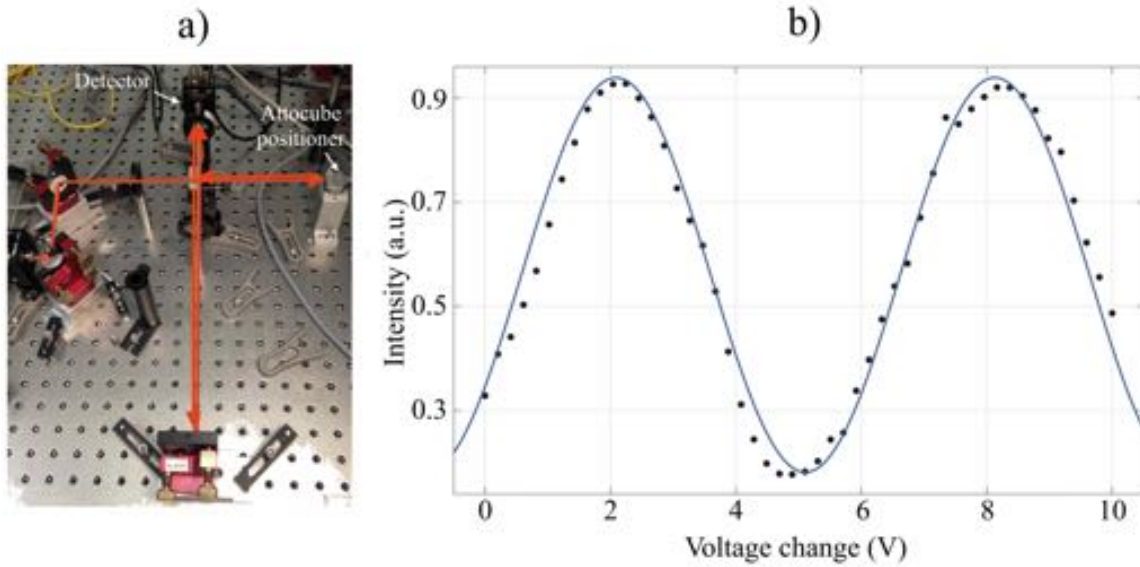


Figure 3.5: a) Michelson interferometer setup for calibrating the Attocube positioner. b) Recorded transmission of the Michelson Interferometer as a function of the change of the Attocube positioner. The black dots correspond to the measured datapoints, the blue line represent the sinusoidal fit.

where, V is the applying voltage and I_0 is the initial intensity. The V^2 term determines that the Attocube positioner behaves quadratically, which we discard for small displacements. For low applied voltage 0.1 V, are equals to 7 nm displacement.

3.4 Measurement of the contact point

In order to calibrate the distance between the resonator and the dielectric substrate, we should find the contacting point (the first point which the dielectric substrate touch the resonator) as an origin. With this origin, the Attocube positioner can provide us the absolute position of the prism or dielectric. Because of the high resistivity ($\approx 3 \times 10^{14} \sigma.m$) of lithium niobate [44], it is not possible to use a electrical current between the dielectric substrate and the resonator to find the contact point. Therefore, we use a sensitive piezoelectric sensor (see Fig.3.6.a).

The piezo is attached on the top of Attocube positioner and connected to oscilloscope to monitor the signal induced by pressure. We apply a triangle voltage to the Autocube positioner by a function generator "Tectronix AFG 3022". In this case Attocube oscillates back and forth as it moves towards the block. When the piezo has not touched the block the voltage that it produces is zero but as soon as the piezo hits the block, a peak will appear in signal (see Fig.3.6). If the Attocube continues moving toward the block the peak height is increased until the block and the Attocube oscillate together. Afterwards, the voltage of piezo will not raise with increasing the voltage of piezo (see Fig. 3.7). The resolution of exact contacting point depends on signal to noise ratio of piezo voltage and it is around 16

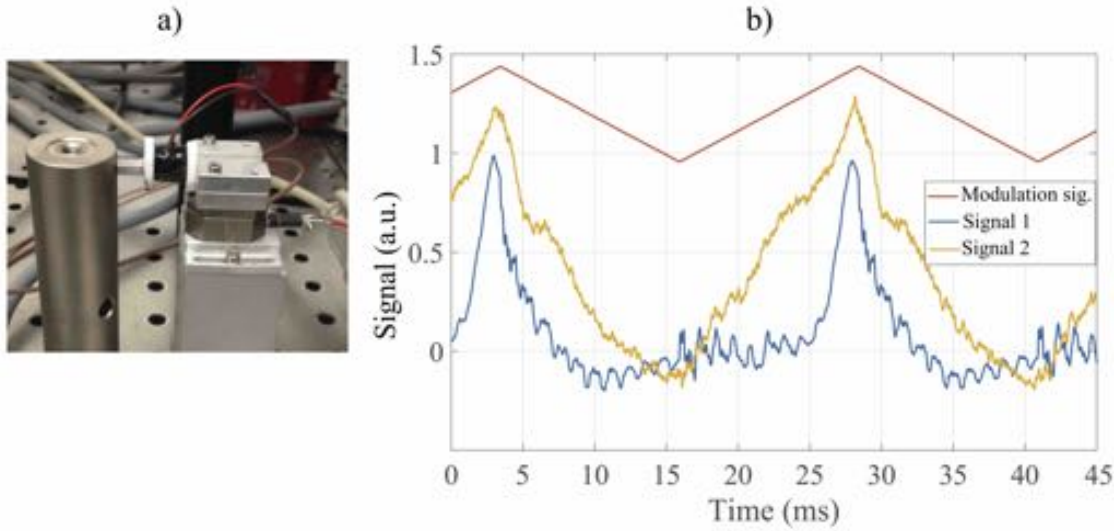


Figure 3.6: a) Setup for measuring the contacting point. We calibrate the distance between the resonator and the dielectric substrate using contacting point as an origin. The piezo (black) is attached to the Attocube and isolated with two pieces of ceramic material. A small piece of aluminum is used as a tip b) The applied voltage to the Attocube is a sawtooth pattern (red trace) function. The output voltage of the piezo shows the contact point. The blue trace shows the contacting of tip and block when the tip is in maximum point of oscillation. When the tip is completely in contact with the block during the oscillation and they oscillate together the maximum of the peak is higher and the decay time is longer (orange trace).

nm in these experiments.

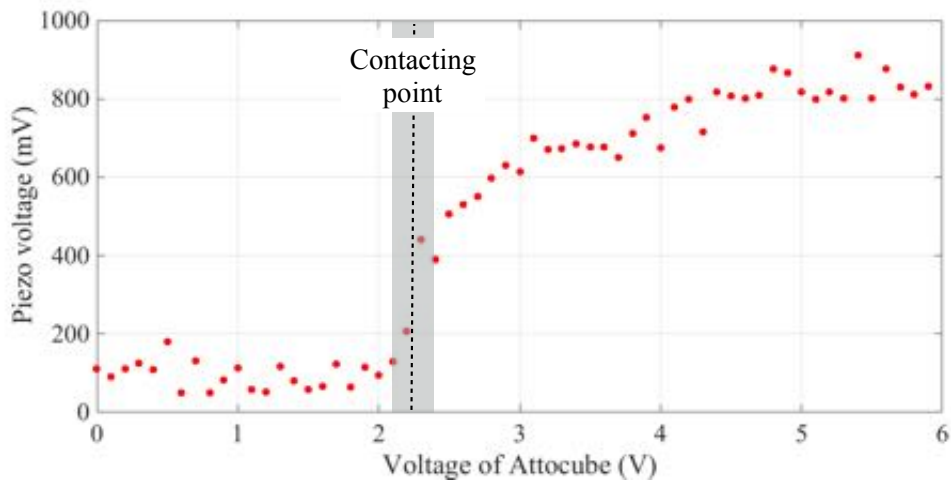


Figure 3.7: The piezo voltage via the Attocube movement toward the block is plotted. The contacting of the piezo and the block induces a voltage in the piezo. The gray rectangular shows the resolution of contacting point and it is 16 nm in this experiment.

3.5 Design of the setup chamber

WGRs are monolithic resonators and therefore very sensitive to temperature drifts and vibrations. To avoid these effects, one should shield the WGMR from environment. Here we design an aluminum vacuum chamber for the WGR with 20 cm length, 19 cm width and 12cm height which it will be used in next generation of our WGMR experiments.

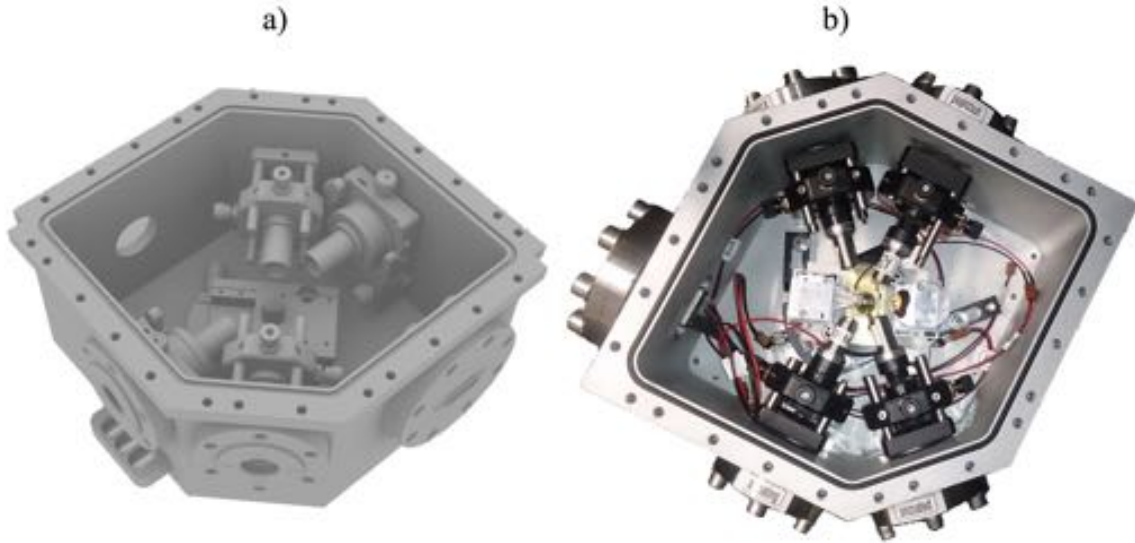


Figure 3.8: The portable aluminum chamber with optomechanical components a) in 3D modeling and b) a picture of setup. The chamber has four windows for the optics and one hole for evacuation. The electronics in the setup is connected via 15 pin D-type feedthrough.

As it is shown in Fig.(3.8), the chamber has four windows for incoming and outgoing light. The windows are set in 135° angle to have maximum coupling of light into the resonator regarding the prism coupling technique. These windows are covered by CF flanges for 10^{-9} bar with ability of changing for different coating window or using fiber coupling port. Inside the chamber there are four commercial lens mounts where each has three degrees of freedom for precise adjustment. The rod which is used in this chamber can be adjusted in different height level.

Temperature inside the chamber is controlled by "Wavelength Electronics LFI-3751" temperature controller, a thermistor (NTC $100k\Omega$) as a sensor and a peltier "UEPT-4151". The sensor and peltier element are located inside the rod to measure and change the temperature of the resonator. The electronic parts are connected to the 15 Pin, D-Type feedthrough on CF flange. The rod is mounted on a ceramic material and isolated from the metallic body of the chamber. This helps to reduce environment temperature effects on the resonator. The lid of chamber is made of transparent Plexy glass which allows us to see inside the chamber and control the setup easier. For this reasons this chamber can be used in many WGMR sensitive experiments.

Chapter 4

Results and discussion

The resonance frequency of WGMR can change with several parameters such as temperature, pressure or evanescent field-material interaction. Tuning the resonance frequency has vast range of applications. The setup has to be stabilized in order to accurately measure the effect of these parameters. Therefore, in the first section, we examine the temperature stability of the system. In the second section we focus on the possibility of the generation of PDC using a 410 nm pump laser in a temperature stabilized lithium niobate WGMR. Finally, we investigate the shift of the resonance frequency when a movable dielectric material approaches the resonator.

4.1 Temperature stabilization with TE and TM modes

As described in section 2.3.5, the differential shifts of the TE and TM mode frequencies allow us to monitor the temperature variation due to different thermal coefficients [39]. For this reason we couple horizontal (TM) and vertical (TE) polarization simultaneously with the setup as shown in Fig.(4.1.a). The radius of resonator is $R = 1.08$ mm and its curvature is $r = 0.16$ mm. In this experiment we use a diode laser at 820 nm and test the temperature stabilization of resonator chamber with measuring TE and TM mode shifts at $109.9^{\circ}C$. The same experiment at $69.9^{\circ}C$ and in vacuum is mentioned in Ref. [45].

The shifts of TE and TM mode in a period of time can be evaluate with two methods. In the first method, differential shifts between the minimum of a TE and a TM mode are analyzed. The corresponding modes are determined in the mode spectrum of WGMR and named case I and case II (see Fig. 4.1.b). The second method uses the technique of cross-correlation of traces with more than 4 GHz range to extract the differential drift between an ensemble TE and TM mode frequencies. In both methods the frequency shifts can convert to changes in temperature regarding Fig.(2.10) (for more information see [45]).

To reduce the effect of pump frequency drifts one can use the second method. Furthermore, in the cross-correlation method there is no need to track selected peaks which can be disturbed during the measurement. The double cross-correlation idea evaluates the cross-correlation of TM and TE mode frequencies at each time-step by correlating the first time-step with each consecutive time-steps. The diagram of this method is shown in Fig.(4.2). Each step of this diagram is also showed in Fig.(4.3). The variation of maxima in double

cross-correlation picture, leads us the temperature drifts of resonator at that time.

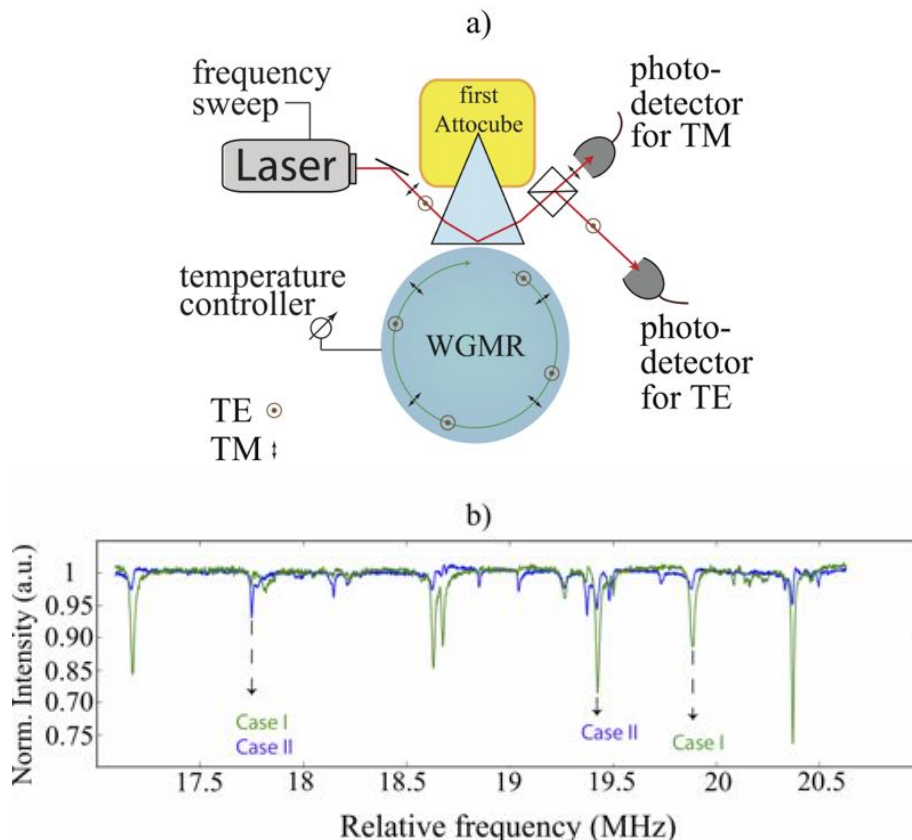


Figure 4.1: a) The main part of the temperature stabilization setup. We set the temperature at 109.9°C . The laser has both TE and TM mode polarization. The outcoupled light is split with PBS and absorbed with different photo detector. b) Normalized TE and TM mode spectra for the whispering gallery resonator. Traces with label case I and case II determine different frequency drifts for different selected TE and TM modes.

In order to measure the frequency shifts, we run the system for one hour with one second time-steps. The captured data is analyzed with both frequency shifts of minimum of the modes and cross-correlation shifts methods in Fig.4.4. In this graph the frequency drifts from the initial frequency is calculated. The different frequency shifts in case I and case II represent the frequency shifts due to the temperature variation depend on number of the modes. But in double cross-correlation method a wide range of frequencies are analyzed and the shifts are independent from the mode number.

As it shown in Fig. 4.4 the frequency shifts in first 20 min is around 2 MHz but it rises to more than 10 MHz in next 40 min. The reason can be the temperature fluctuations in the laboratory (see Fig.4.5). The fluctuations are mainly $\pm 1^{\circ}\text{C}$ at 21.5°C but the temperature fluctuation raises at specific hours because of the traffic in the lab. Another reason might be the limited sensitivity of the temperature sensor. If the temperature fluctuation is smaller than the sensitivity of the sensor, the controller does not activate the heater.

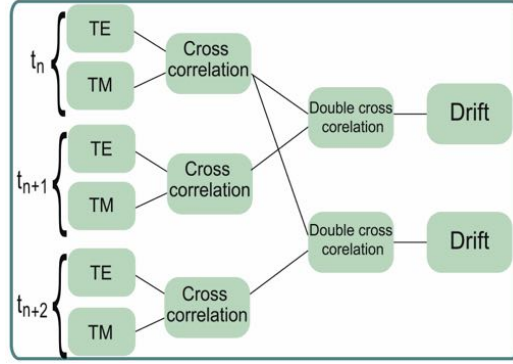


Figure 4.2: The diagram of the data processing via cross-correlation. At each time step TE and TM spectra are cross-correlated. In the next step the cross-correlations are correlated again to determine the drifts.

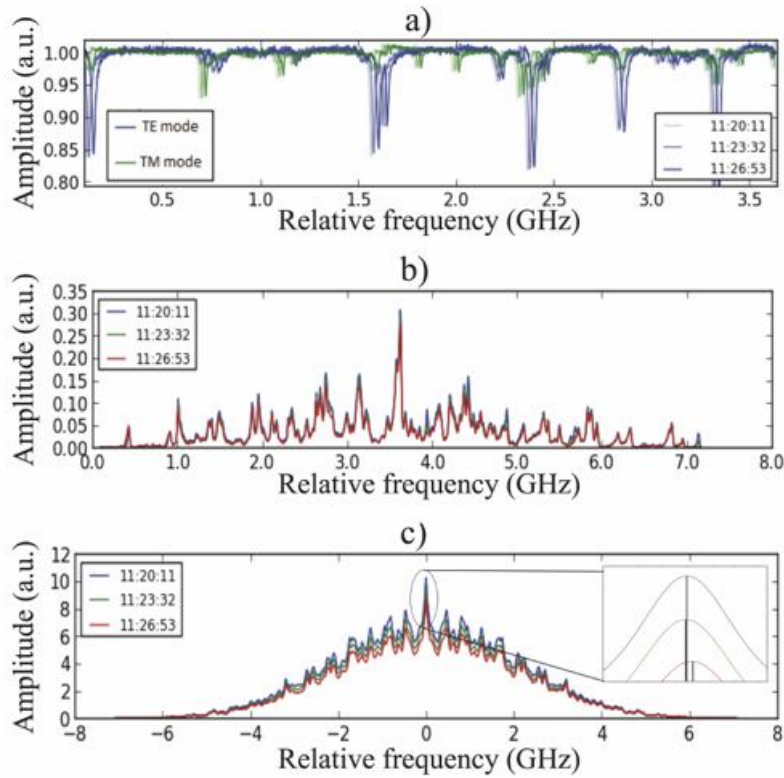


Figure 4.3: a) We record 3 time steps of the TE and TM modes spectrum. b) We cross-correlate the corresponding TE and TM modes at each time steps. c) Double Cross-correlation of mods between first time step and the other next steps are shown. Inset: The zoom of peak shows the frequency drifts from central frequency.

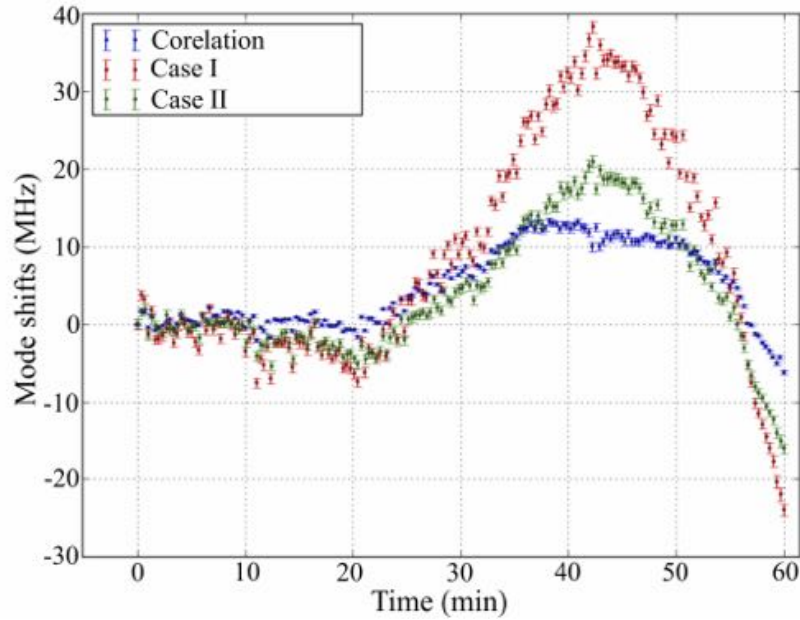


Figure 4.4: We calculate frequency drifts from the cross correlations method and the direct differential frequency of case I and case II. Different resonance frequency shifts for the case I and case II indicate each mode number can shifts differently with thermal changes. Both methods show similar behavior but the frequency drifts of the cross correlation method diverges less and it is not dependent on the mode number. Here, 10 MHz frequency shift is approximately equal to 1 mK temperature drift (see Fig. 2.10).

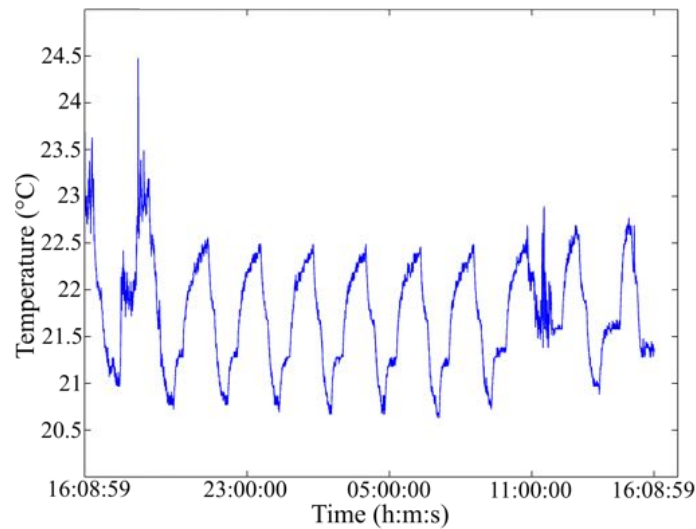


Figure 4.5: The laboratory temperature fluctuation in 24 hours. The temperature fluctuate roughly 2 °C at each 2 hours time interval. At 17:00 and 12:00, the traffic in lab is heavy and the lab door open and close a lot. This will raise the fluctuation.

4.2 Towards parametric down conversion using blue light

Lithium niobate is a widely-used nonlinear crystal to generate parametric down conversion at 532 nm pump light with low power threshold (few μW) [38]. But generating a PDC in ultra violet (UV) regime is challenging. In theory, this process is possible, however, the conversion efficiency of that is extremely low. The temperature dependence of PDC for 410 nm pump light is shown in Fig.(4.6). This graph is plotted with a program which has been written in QIV group based on calculation in section 2.3.4, 2.3.2 and Sellmeier equation (2.17). The generated signal has a wavelength around 500 nm and it is almost temperature independent. As shown in this graph, the efficiency of PDC at 410 nm is low.

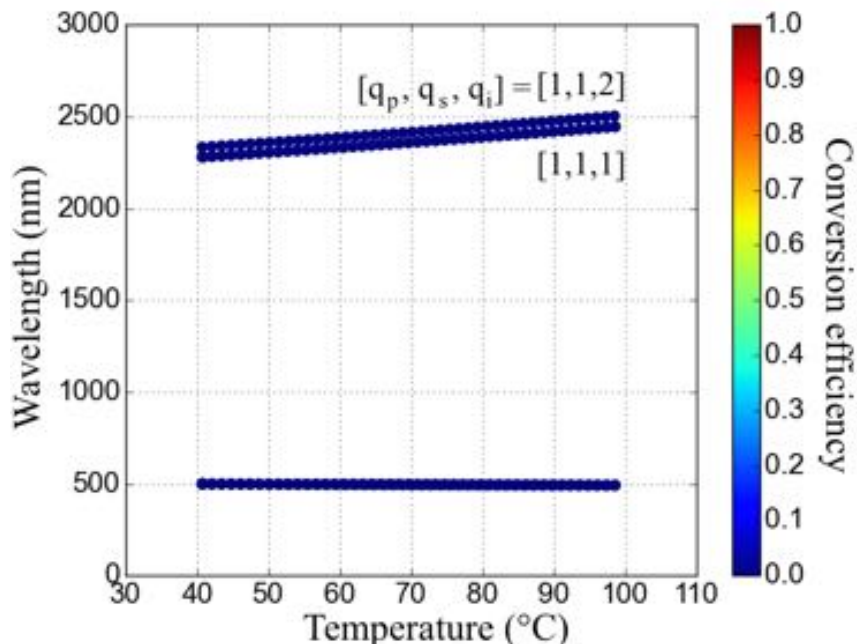


Figure 4.6: Numerical simulations of phase-matching solutions between different WGMs with different radial mode numbers q . Here, the angular mode number p is zero.

In this experiment we use 410 nm pump laser (SHG of 820 nm) with the maximum power of 350 mW and the effective power of 35 mW before the resonator chamber. The setup is similar to Fig.(4.1.b) as described before with Fabry-Perot interferometer as a frequency reference. Equation 2.54 represents that the PDC power threshold is highly depend on the quality factor of the resonator for the pump and the signal. According to [38] the experimental power threshold for 532 nm is at least 3 orders of magnitude larger than theoretical prediction. The reason can be the resonator geometry. The calculation has been done for spherical resonator but here we have a semi-spherical resonator. To understand the power threshold at 410 nm, first we calculate it numerically. The graph of lithium niobate absorption coefficients points out the lithium niobate absorption in 410 nm is higher than

532 nm [46]. Considering the Q-factor Eq.(2.47), one can plot the Q-factor versus prism coupling distance for different wavelengths numerically (see Fig.2.9).

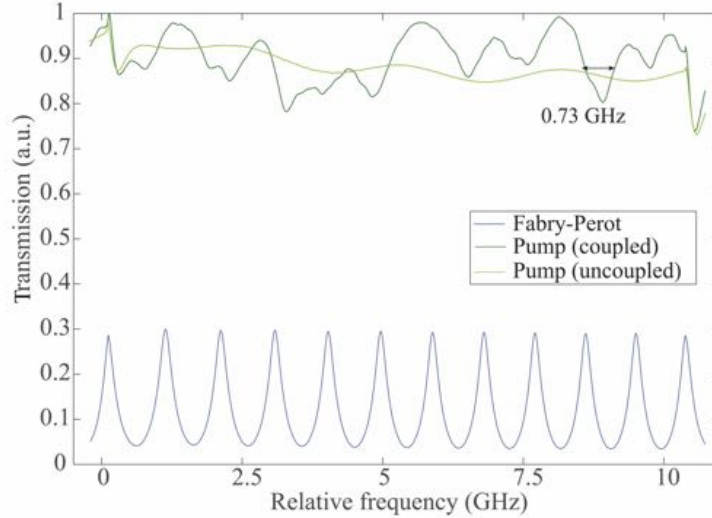


Figure 4.7: Mode spectrum of lithium niobate WGR at a wavelength of 410 nm. The green line shows the laser sweeping when it is not coupled to the WGR. The red line is the spectrum of coupled light to the resonator. finding the fundamental mode is difficult because the modes are highly overlapped. Fabry-Perot is used as a frequency source in the lower trace.

The numerical Q-factor for 500 nm (signal) at the critical coupling point is around 2.2×10^7 and for 410 nm is 1.03×10^7 . But finding the Q-factor at 410 nm in experiment is challenging. Because of the modes are overlapped in critical coupling region, finding the fundamental mode is difficult. This mode overlapping cause the mode bandwidth seems wider and therefore the measurable Q-factor can have smaller amount than the real Q-factor. The spectrum of resonator with 10 GHz sweeping is shown in Fig.(4.7). The experimental Q-factor for 410 nm pump light is roughly 1.01×10^6 . Calculating the power threshold with effective quadratic nonlinearity ($\chi^{(2)} = 17 \times 10^{-12}$ [m/V]) and overlap integral ($\sigma = 2.64 \times 10^9$ m^{-3}) gives the value of $55.1 \mu W$. According to three orders of magnitude difference between theory and experimental result [38] observed in an earlier work, this value should be 55.1 mW. The maximum effective power in this experiment is 35 mW before the aluminum chamber and we should also consider the losses in the chamber. In order to achieve PDC we should increase the effective power or the Q-factor of pump laser at 410 nm.

4.3 Frequency tuning of whispering-gallery modes

In this section we are trying to explain the frequency tuning of the resonator with movable dielectric material. The dielectric substrate can tune the resonance frequency by applying a pressure on the resonator or the interaction of evanescent field and substrate. The temperature changes which is not desirable in this experiment can shift the resonance frequency as well. In all the experiments in this section we used Matlab code to control the position of

second Attocube and evaluate the data. In data evaluation process, by selecting a mode, the program will plot the bandwidth, frequency shifts and reflected intensity of the mode while the Attocube is moving.

4.3.1 Local temperature variations

In this experiment we used a diode laser with the infrared light at a wavelength of 820 nm. The WGR is z-cut lithium niobate with the resonator radius $R=1.6$ mm and the curvature radius $r = 0.16$ mm. In order to align the system we use green light at 532 nm. Green light has florescent effect inside the diamond which could help to follow the light direction inside the prism and find the proper incident angle. After this rough alignment, we switch the laser into IR and align the system for this laser precisely. The scheme of main part of setup and the side view of the resonator and the dielectric substrate is shown in Fig.(4.8).

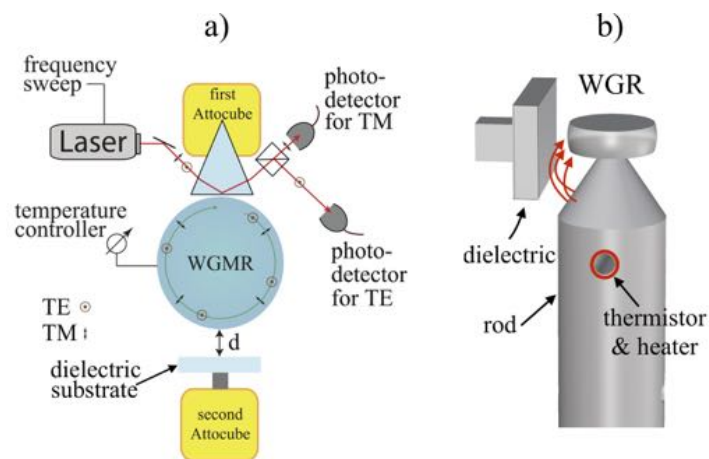


Figure 4.8: a) Scheme of the frequency tuning setup with movable dielectric material made of zinc oxide. The temperature is set above room temperature ($45^{\circ}C$). b) Side view of the setup. The dielectric blocks the convection (red arrows) which causes the resonator to heat up. The thermistor under the resonator does not feel this local warming because of its distance to the top of the rod and as a result the temperature controller will not compensate the temperature change.

The second Attocube moves towards the resonator stepwise. Because of stranger effect and easier calculation in theory we try to select the fundamental mode. But finding this mode is not always straightforward. We can guess the fundamental mode or a mode with small mode number from coupling contrast and bandwidth (see Fig.4.9.a). We measure the mode shifts for TE and TM via coupling distance by applying a voltage to the second Attocube.

Applying 21 V to the Attocube corresponds to 1400 nm displacement. The graph of frequency shifts versus Attocube displacement is shown in Fig.(4.9.b) at $45^{\circ}C$. This graph illustrates that the mode is shifted even when the dielectric substrate moves far from the resonator (around $1 \mu m$ far). The possible scenario is in the presence of dielectric substrate, the convection is influenced by the surface of dielectric substrate. This can change the

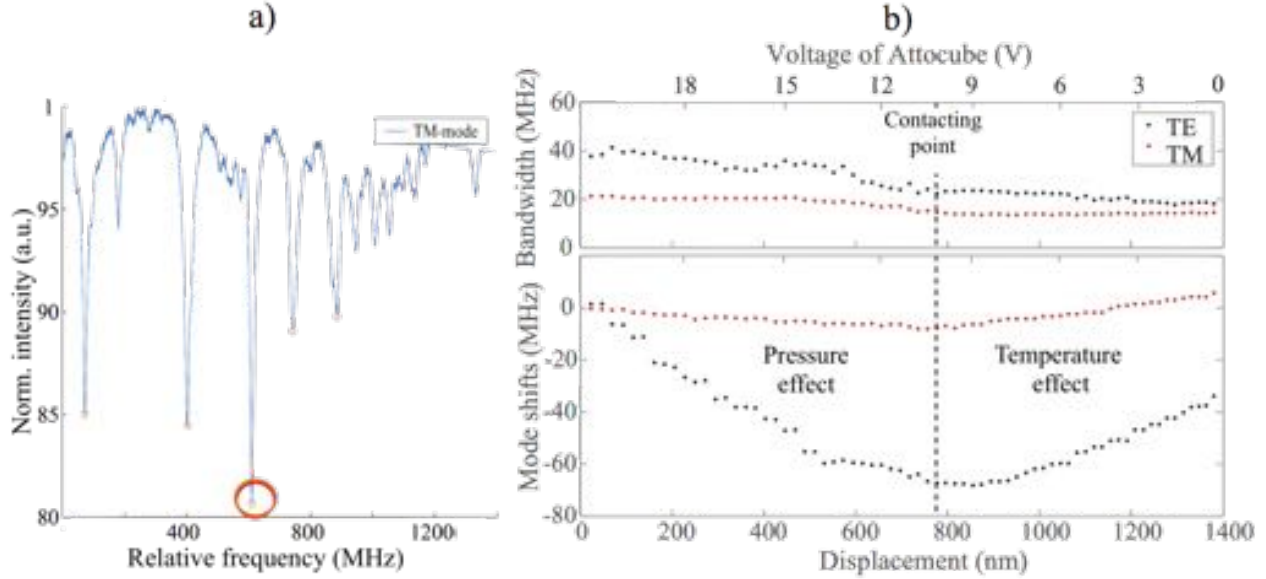


Figure 4.9: a) We assume the marked mode is a fundamental mode in the WGM spectrum while it has the narrowest bandwidth and the maximum coupling contrast. b) The frequency shifts of the selected mode in each Attocube moving steps. The vertical dashed line shows the probable contacting point. The temperature variations can shift the resonance frequency due to the dielectric substrate movement. Before the contacting point, in temperature effect area, the Attocube voltage is directly proportional to the dielectric substrate displacement ($\approx 69 \text{ nm/V}$). The mode shifts in pressure effect area most probably arises from the dielectric substrate pressure on the resonator.

temperature of the WGR and heat up the upper part of the rod locally. While the thermistor is inside the rod and is located 14 mm lower from its tip, the thermistor cannot recognize these changes and will not compensate the temperature difference (see Fig.4.8.b). With moving the dielectric substrate towards the resonator, the temperature changes and it shifts the resonance frequency as well.

In Fig.(4.9) the red shift turns to blue shift around the vertical dashed line. This can point out either the dielectric substrate hit the resonator or the WGR evanescent field interact with the dielectric substrate. The same experiments have been done at 30°C , 60°C and 75°C and the results is obtained .

4.3.2 Frequency shifts at room temperature

One way to avoid local temperature drift is measuring the data at room temperature and without temperature controller. While the resonator is completely shielded with the chamber, room temperature variations has a minor effect on the resonator. In Fig.(4.10) the mode shifts via voltage of Attocube at room temperature is illustrated. When voltage of the Attocube is zero, the distance between the WGR and the dielectric substrate is much greater than evanescent field of the WGR. By applying voltage to the Attocube this distance is reduced until the dielectric substrate contacts the resonator. Despite Fig. 4.9.b, in

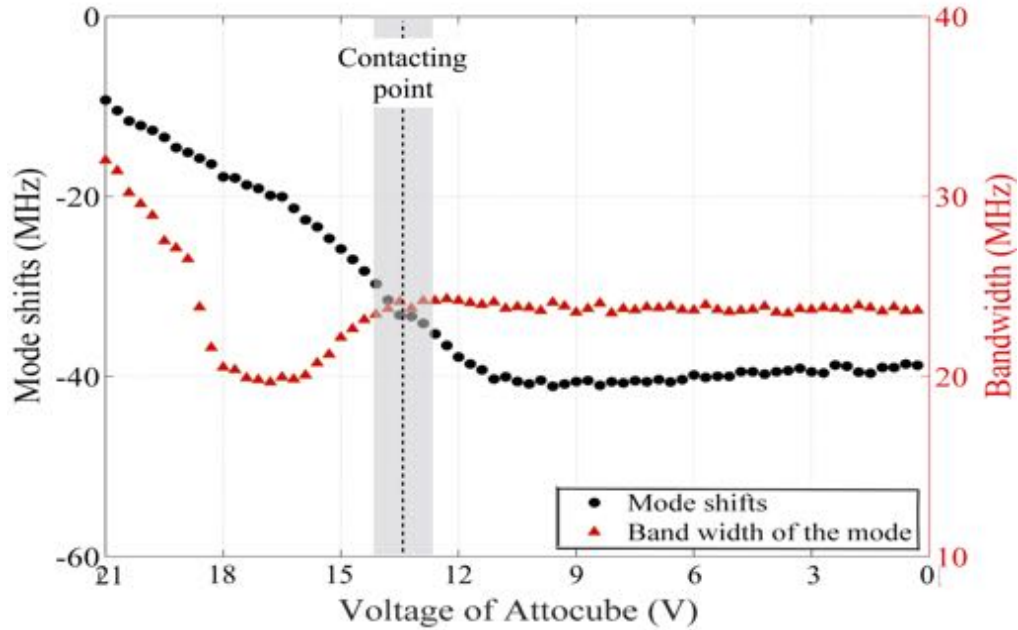


Figure 4.10: The TE mode shifts versus the position of dielectric substrate is plotted. The mode shifts is saturated when the dielectric substrate is far from the resonator at room temperature. The laser drifts can slightly shift the mode in this region. We consider the point in which the bandwidth is changed as a contacting point. The mode shifts before the contacting point can be described by evanescent field effect.

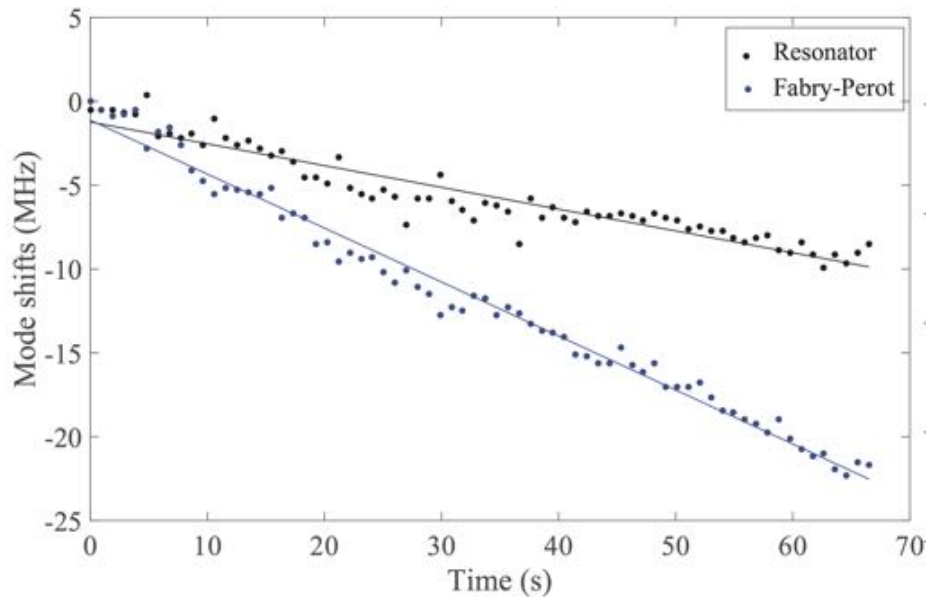


Figure 4.11: Frequency shifts in Fabry-Perot and WGR due to temperature and laser central frequency drifts. The slopes of linear fitting in a stable temperature must be the same.

this measurement there is a very small shift when the dielectric substrate is far from the

resonator. This can reinforce the hypothesis that temperature controller affects the mode shifts when the on dielectric substrate is moving towards the resonator.

The small mode shift when the distance between the dielectric substrate and the WGR is great can arise from the laser drift in time. Fig. 4.11 determines the mode shifts in the WGR and Fabry-Perot. In order to estimate the laser frequency drift, we compare the Fabry-Perot mode shifts with resonator mode shifts. Then with linear fit, we can find the estimate value of laser drifts in period of time.

If the dielectric substrate touch the resonator and push it toward the coupling prism, the coupling distance will be changed and as a result the bandwidth of the mode will also change. Therefore, We consider the point in which the bandwidth start to shift as a contacting point. The mode shifts before this point can be caused by the effect of evanescent field and the shifts after the contacting point can be due to the pressure effect.

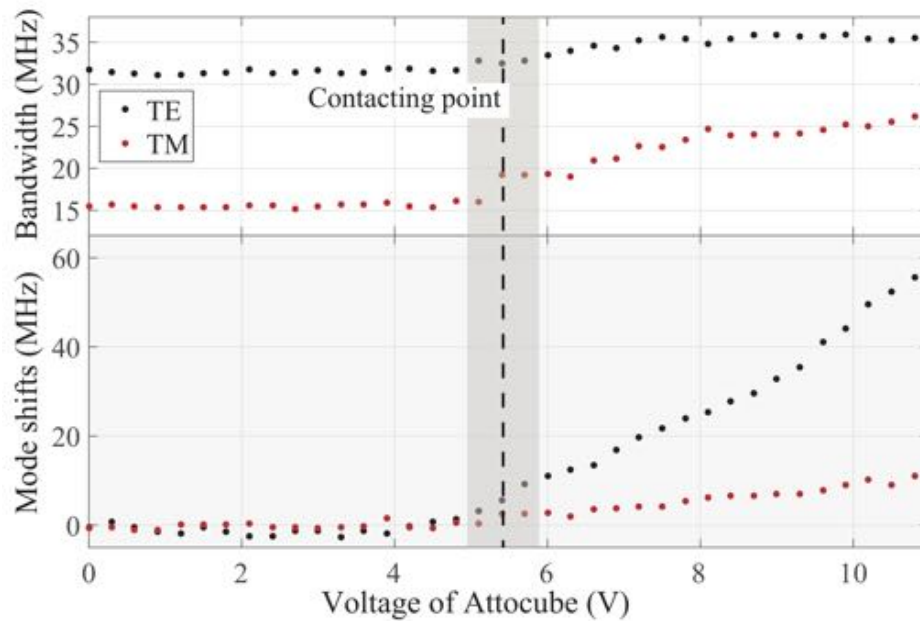


Figure 4.12: The position dependent shifts of resonance frequencies of a WGMR with radius $R = 1.6 \text{ mm}$ at a wavelength of 820 nm . The modes with different polarization shift in a same direction.

The different TE and TM modes are shifted in the same direction when the dielectric substrate moves toward the resonator (see Fig. 4.12). The shift before the assumed contact point is not more than 10 MHz.

One important point at room temperature experiment is the system must be in equilibrium with its surrounding. This process can take a quite long time (over 6 hours) if the system was in higher or lower temperature before.

Movable coupling prism

The resonance frequency can also shifts when we are trying to couple the resonator with movable diamond coupling prism. Regarding to size of the chamber, we could not use the piezo to find the contacting point but one can approximately find this point with variations in bandwidth of a mode (see Fig.4.1).

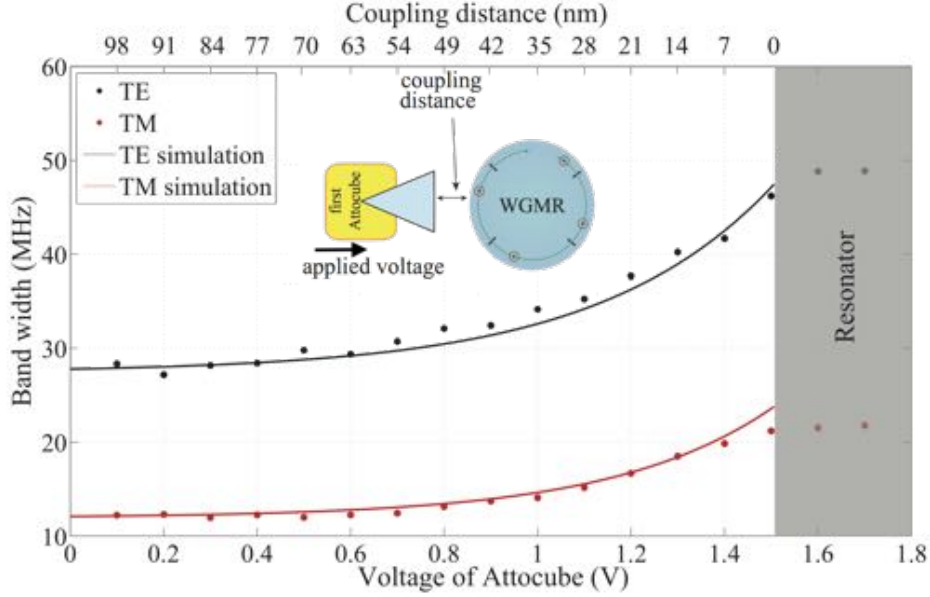


Figure 4.13: We plot the bandwidth of TE and TM modes of the WGMR ($R = 1.6$ mm) against the displacement of the coupling prism. We can extract the contacting point by a fitting from Eq.(4.2) to the TE and TM experimental data. Here the fitting parameter A for TE mode is one. This means this resonator properties are quite similar to spherical resonator. This value is 0.83 for the TM mode.

The mode bandwidth rises exponentially with the distance between the prism and the WGR in evanescent field and can be calculated as:

$$\gamma = \gamma_i + \gamma_c \quad (4.1)$$

where γ_i is the intrinsic bandwidth and is a constant value. γ_c is the loading bandwidth and derives from Eq.(2.49, 2.33). The Eq.(4.1) can be applied for spheroidal resonator with a constant coefficient A as a factor of geometrical changes:

$$\gamma = const. + A\gamma_c. \quad (4.2)$$

With applying the simulated data from the theory we can estimate the position of the resonator. This can help us to find the prism coupling mode shifts before it touch the WGR (see Fig.4.14). Here the maximum mode shifts is roughly 6 MHz for TM.

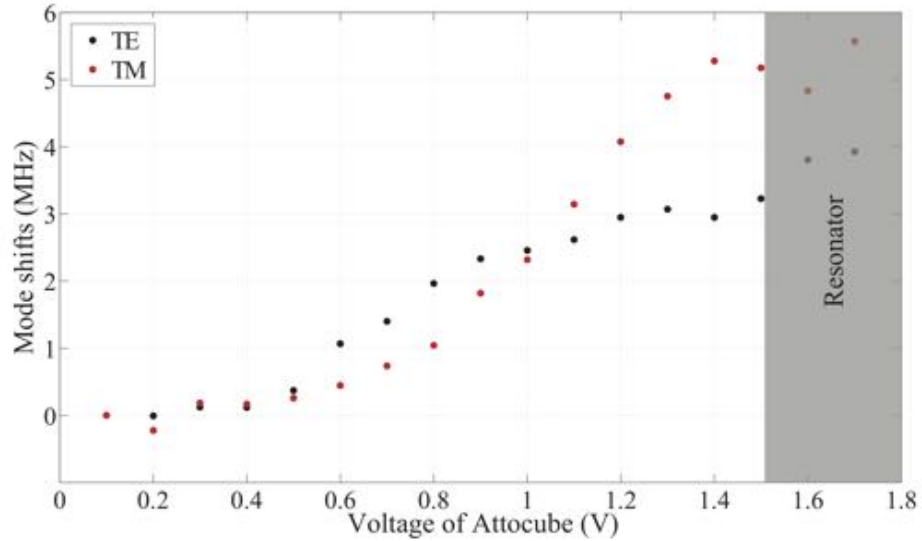


Figure 4.14: The resonance frequency of the TE and TM modes shifts with movable coupling prism. These shifting are caused by moving the dielectric substrate in the evanescent field of the WGR. As theory predicted, both shifts are in a same direction.

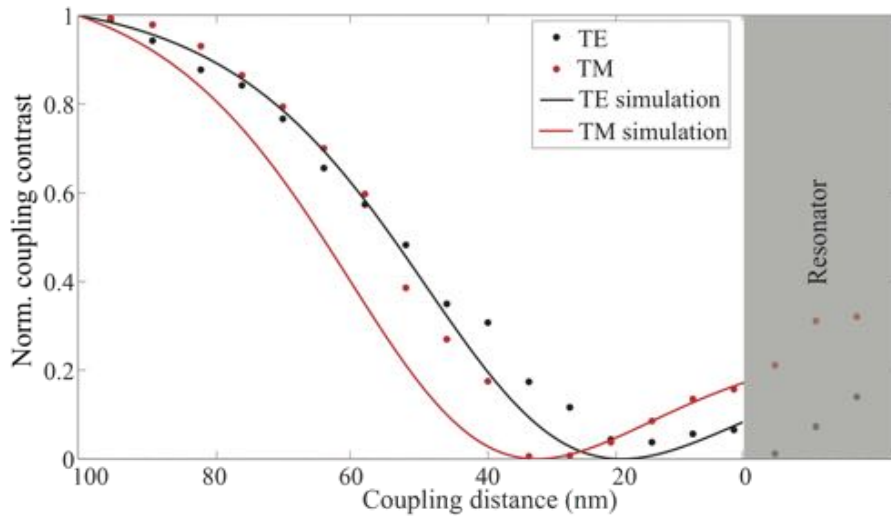


Figure 4.15: The normalized coupling contrast of TE and TM modes against the traveling distance of the coupling prism. We extract the critical coupling distance for TE (20 nm) and TM (34 nm) by fitting Eq.(2.46) to the data. The modal overlap between the incident field in the prism and the propagating mode in the resonator A is 0.4 in this case. The fitting mismatch for TM mode can be caused by the step jump of the Attocube during the experiment.

As we mentioned in section (2.3.3) the normalized reflected intensity is zero in critical coupling and is one when the prism is far away. To find out the critical coupling distance one can plot the reflected intensity value for different coupling distance (see Fig.4.15). Here

the numerical graph (see Eq.2.46) does not fit to the experimental data but it illustrates the same behavior. This mismatch can be result of the Attocube jump in steps during the move. The other reason is the coupling contrast for TE and TM is around 14 % and 22 %, respectively in the critical coupling distance. Therefore, the coupling contrast in each step is rather small and they are not clearly distinguishable and can increase the measurement error during the experiment. The graph approximately can show us the critical coupling distance for TE and TM modes which is important for a efficient coupling in WGMR.

In this experiment, we were able to confirm the interaction of evanescent field with any material can change the resonance frequency. This can help us to analyze the WGMR spectrum in different coupling ratio. Additionally with moving a dielectric in the evanescent field we can finely tune the resonator without any mechanical or geometrical changes in the resonator.

4.3.3 Pressure tuning by movable dielectric substrate

For two reasons the resonance frequency can shift when substrate is hundreds of nonometer far form the resonator: 1. The temperature effects and 2. The laser frequency drifts. Due to the length of field decay outside the WGR (≈ 110 nm), the evanescent filed cannot affect the resonance frequency in a range of 600 nm displacement (from 21 to 12 V in Fig.4.10). As a result, the mode shifts in this region cannot be only because of the evanescent field effect.

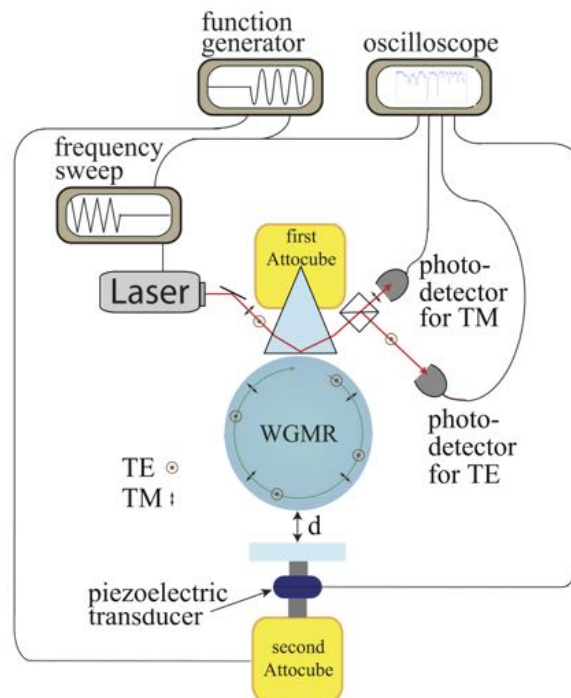


Figure 4.16: The pressure tuning setup using piezoelectric to find the contacting point. The laser is swept over an adjustable bandwidth for 20 ms and set to central frequency for 80 ms. The second Attocube oscillate after 35 ms delay. After this 100 ms, the Attocube moves forward one step (0.1 V). This process is repeated for the given Attocube steps iterations.

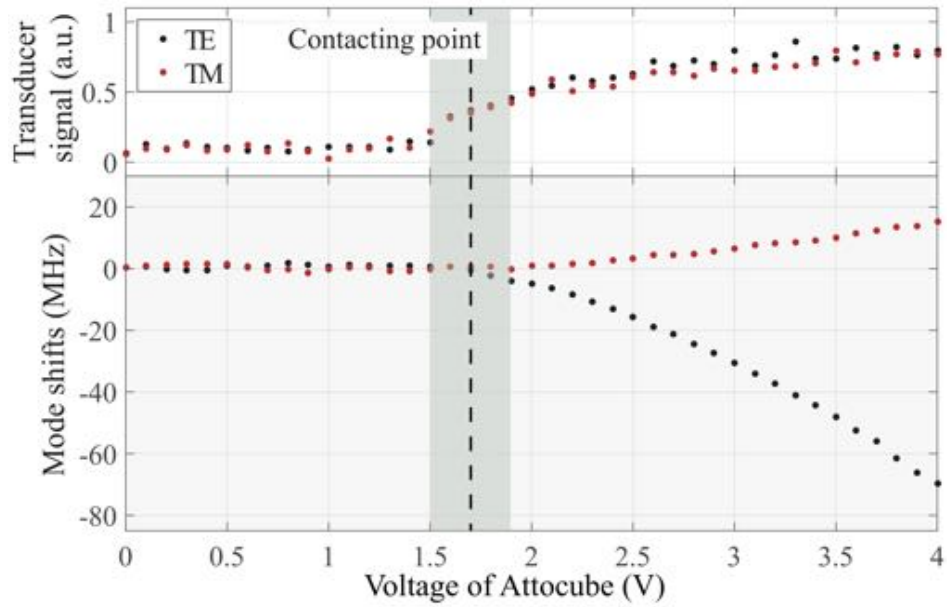


Figure 4.17: We measure the position dependent shifts of resonance frequencies of TE and TM modes at a wavelength of 532 nm. The contacting point is measured with a piezoelectric transducer having an approximate accuracy of 0.23 V (16 nm). Small nonlinear frequency shifts for TE and TM modes around the contacting point are observed, which we attribute them to a polarization of the dielectric substrate by WGMR evanescent fields. For higher voltages, we measure nearly linear frequency shifts as we expected from section (2.2.3). Here the shifts are in different directions regarding the mode polarization.

We consider on situation that the dielectric substrate touches the resonator and presses it. In order to study the pressure effects, we should find the exact contacting point with the method which is explained in section (3.4). In this experiment we use another setup shielded with polyethylene foam. The laser light is SHG of Nd-YAG (green light) at 532 nm and we work with the z-cut lithium nionate resonator with $R = 2.5$ mm and $r = 0.58$ mm [9]. Here, the ZnO dielectric substrate is glued to an aluminum tip. The laser, function generator and oscilloscope, are connected to the laser trigger (see Fig.(4.16)). The laser sweeping time is set to 20 ms in the current experiment. After the sweeping, the laser frequency is set to the central frequency for 80 ms. At this time, the function generator starts to sweep with 15 ms delay. Indeed, the function generator has 35 ms delay and sweeps 20 ms. This generator sends 15 mV signal to the Attocube controller. The signal applied by factor of 15 and it is applied to the second Attocube positioner. The Attocube can oscillate around 16 nm with this voltage. This is enough to see the signal when the piezo hit the resonator. The intensity of piezo signal in each step is plotted in Fig.(4.17) This voltage will saturate when the dielectric substrate is completely in contact with resonator during the oscillation.

The frequency shifts of TE and TM modes are measured with moving the second Attocube towards the resonator. Here the TE mode has a red shift but the TM mode shifts into blue. According to the section (2.3.6) the shifts should be in same direction for hydrostatic

pressure. Interestingly, in the previous setup these shifts were in the same direction for different polarizations (see Fig. 4.12).

The asymmetric applied pressure or different order of the modes can be the reason of different shift directions of TE and TM modes. In Ref. [47] symmetric pressure on a solid polystyrene microsphere causes the shifts of the modes. These shifts can be in same or different direction due to the mode numbers. The paper mentioned, after a specific number the mode shifts direction will change. But this number is $p \approx 150$ for polystyrene microspheres. In our experiment the angular mode number cannot be near 150. But it is possible for lithium niobate this number is different from polystyrene. To understand this critical angular mode number of lithium niobate one should solve the same problem with this material.

4.3.4 Evanescent field tuning by movable dielectric substrate

The dielectric substrate can have interact with the evanescent field of WGMR according to theory and experiments [1]. The movable dielectric substrate in the evanescent field change the resonance frequency of the resonator. The Fig.(4.12) illustrates the evanescent field

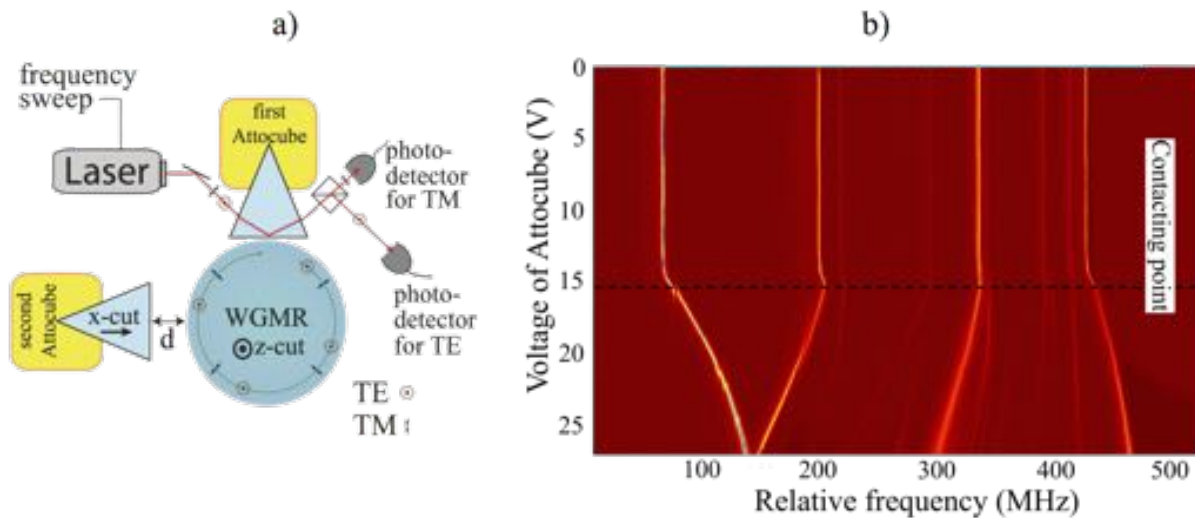


Figure 4.18: a) The evanescent field tuning setup with movable x-cut lithium niobate prism. The s-polarized light can outcouple into a second x-cut prism made of lithium niobate but the p-polarized has a higher refractive index in the WGMR than the second prism and it cannot be coupled out with the second prism. b) The resonance frequency of TM modes (p-polarized) are changed inside the evanescent field with the position of the movable second prism. After the assumed contact point, the different modes are moving in different directions depending on their mode numbers. Some modes are shifted before the contact point, which we attribute to the evanescent field effect. These shifts appear as a kink in the contact point area.

has a minor influence on resonance frequency. Hence, we used a high Q-factor resonator and selected the mode with 2.2 MHz bandwidth to see the mode shifts better. Here, we used a

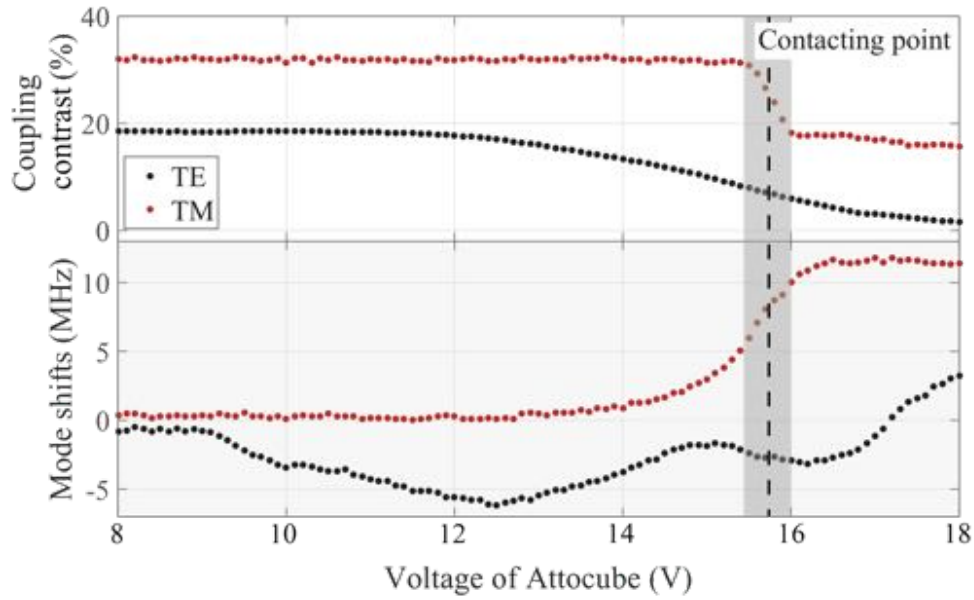


Figure 4.19: The changes in coupling contrast and resonance frequency (mode shifts) for TE and TM modes. The contacting point is selected with the drastic change in coupling contrast. The TM mode shifts exponentially in evanescent field of WGMR around 6 MHz. The TE mode coupling contrast is decreased gradually due to second prism outcoupling and the resonance frequency shifts does not considerable.

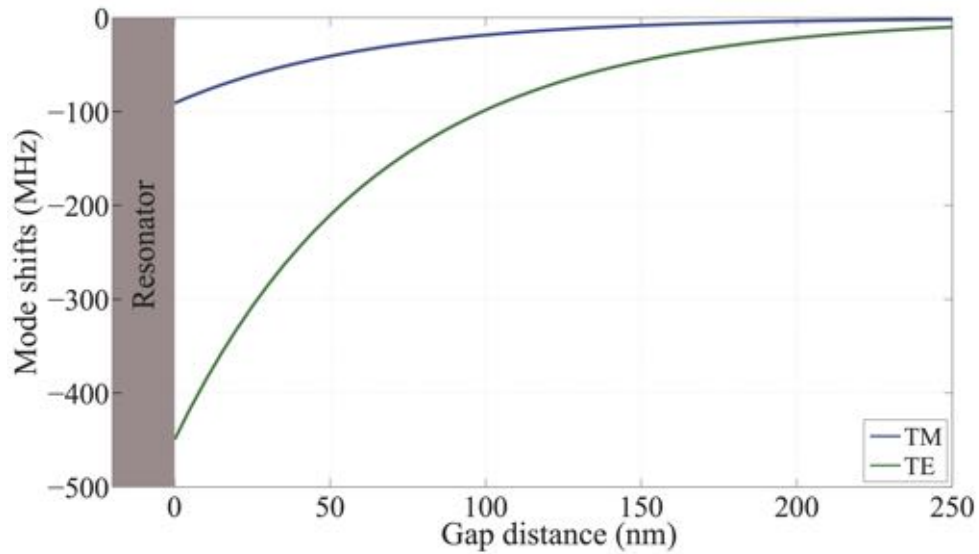


Figure 4.20: The numerical simulation of the evanescent field effects. The TE and TM mode shifts are a factor of 10 greater than the experimental results. Both TE and TM modes are shifting in same direction (red shift).

WGMR made of lithium niobate with $R=2.13$ mm and diode laser at 1550 nm wavelength. To avoid pushing the resonator to prism side and changing the coupling distance, we put the substrate with 90° angle to the prism. Here, the dielectric substrate is an x-cut lithium niobate prism (see Fig.4.18.a). This experiment has been done by Florian Sedlmeir.

In the spectrum of p-polarization light, there are some modes where drifts in different direction as shown in Fig.(4.18.b). The graph elaborate that the pressure can drifts the modes in different directions due to their mode numbers. Here, some modes have a kink before they start to drift linearly.

We investigate the region which the kink appears. In Fig.(4.19), the coupling contrast and the shifts of TE and TM modes are plotted. The drastic change in coupling contrast of TM mode indicates that the substrate and the resonator are in contact. For TE mode the light is outcoupled with x-cut lithium niobate (second prism). Therefore, the coupling contrast has gradually decreased. This phenomena is known as selective coupling. The s-polarized light into the x-cut lithium niobate prism and z-cut WGR made of same material produces TM and TE modes, respectively. TE modes in resonator (z-cut lithium niobate). Due to the polarization dependence of refractive index in lithium niobat (see section 2.2), the refractive index of the TE modes is smaller than the TM. As stated in Eq.(2.43) the light can only couple when n_p is greater than n_s . Therefore the TE mode can couple out with the x-cut prism but TM mode cannot outcoupled.

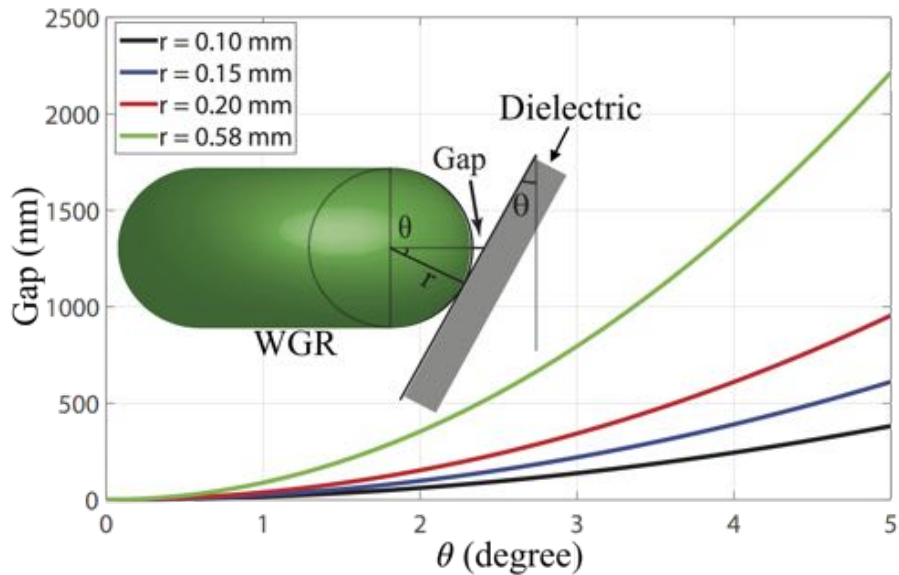


Figure 4.21: A tilt of substrate or resonator can make a gap in equatorial position of a WGR when the substrate touches the resonator. The length of this gap depends of tilting angle and the resonator's small radius (radius of curvature). This length can be more than the length of the evanescent field of the mode.

The frequency shifts due to the evanescent field is clearly more than 5 MHz. But this value according to the theory should be 100 MHz (see Fig.4.20). Below we will discuss about few parameters which can cause this difference.

- The theory shows the frequency shifts in the fundamental mode but the mode which we have selected can be a higher order mode with less intensity and shorter decay distance.
- The WGMR and the dielectric substrate must be completely orthogonal to each other. Any tilt of WGMR or dielectric material can cause a gap between them when the dielectric substrate touch the resonator. In Fig.(4.21) we determine the gap after touching for different tilting angle of the substrate. This gap can be more than the length of field decay if the dielectric substrate is tilted only 2 degree.
- In theory, the resonator has a cylindrical geometry. This means the whole surface of resonator in polar direction interact with substrate but in spherical geometry the interaction surface will decrease due to rim curvature.

Although the mode is shifted 5 to 10 MHz in this experiment but we are able to tune the frequency continuously and without mechanical interaction with this method.

It is remarkable to know that by coupling the light with one prism we can in principle always steer the beams such that we find a mode that couples well, but if we try to couple out the same mode with a second prism the tilt of this second prism has to match with the first prism.

Chapter 5

Conclusion and outlook

Frequency tuning of WGMR can be used in spontaneous parametric down conversion (SPDC) experiment to tune the single signal and single idler photons continuously. This tuning has also many applications in atomic transition and the quantum communication.

In this thesis we investigated the frequency tuning of the WGMR via a movable dielectric substrate. The WGMR in this experiment is a spheroidal resonator made of lithium niobate. The movable dielectric is a plane surface glass coated by a layer of zinc oxide with 100 nm thickness or a x-cut lithium niobate prism. The dielectric substrate could interact with evanescent field of WGMR and manipulate the resonance frequency (up to 10 MHz for large disc $R=2.1$ mm). According to the theory and experimental results (see Fig.4.19) the resonance frequency will exponentially increase with decreasing the distance between the dielectric substrate and the WGR. When the movable dielectric substrate touches the resonator, it will change the elasticity and geometry of the resonator. Applying external pressure on the resonator by moving the dielectric substrate forward can tune the mode frequency in a range of few GHz [9]. In contrast to evanescent field tuning, the resonance frequencies are changing linearly with pressure. The direction of the mode shift (red or blue shift) depends on the number of WGMs. The mode shift changes its slope as the angular mode number p is higher than critical p number [47]. This p mode number is still not calculated for lithium niobate WGR.

The resonance frequency highly depends on temperature. We measured the temperature stability of the system with differential shift of individual TM and TE modes. The TE and TM modes frequencies have different temperature coefficients in lithium niobate WGMR. Their differential shift provides a sensitive way to measure of the temperature variations. The stability of the temperature in this case was less than 1 mK during 20 minutes.

In order to have a reliable measurement we redesigned an aluminum chamber to shield the resonator from surrounding changes. This can improve the stability of system and make the setup portable.

As a first application of our WGR setup we investigated the PDC process for lithium niobate (with 5% Mg doped) resonator in blue light (410 nm wavelength). The maximum power which we pumped into the resonator was around 38 mW. According to the theory and in comparison with the experimental results at 532 nm wavelength (green light), the power threshold should have been more than 55 mW. This threshold is much higher than the

value for green light. One reason for this difference is higher intrinsic absorption of lithium niobate at blue light.

As a future plan one can find the pressure effect for specific mode number. This has been done for uniaxial pressure on solid polystyrene microspheres in theory and experiment [47]. With calibrating the mode shifts via pressure, the WGMR can be used as a sensitive pressure sensor. The relation between pressure and the mode number can also help to identify the modes. In this thesis, the frequency shift of interaction between WGR's evanescent field and movable dielectric substrate was simulated for a cylindrical resonator disc. A future analysis of spheroidal WGMR can explain our measured shifts. Furthermore, the dielectric substrate tilting can reduce interaction for the fundamental modes. By adjusting the resonator, coupling prism and dielectric substrate with more accurate device and controlling them with more degrees of freedom we can avoid such experimental errors.

Acknowledgments

I would like to express my gratitude to Prof. Gerd Leuchs for giving me the possibility to work as a master student in his division and Dr. Christoph Marquardt who supervised me during this project on his research group.

I can not neglect the great and devoted guidance of Gerhard Schunk who is not only a supervisor but also a good colleague and friend. His guidance helped me in all the time of research and writing of this thesis.

My sincere thanks also goes to Prof. Arno Rauschenbeutel as a local supervisor in Vienna university of technology who helped me to join Max Planck research group.

Also I thank my friends Joanna Janas, Florian Sedlmeir, Ulrich Vogel, Pooria Hosseini, Alexander Otterpohl and Golnoosh Shafiee in the Max Planck institute for the science of light for their ideas and helps.

Most importantly, none of this would have been possible without the love and patience of my family and my partner.

Bibliography

- [1] S. Arnold, M. Khoshsima, I. Teraoka, S. Holler, and F. Vollmer. Shift of whispering-gallery modes in microspheres by protein adsorption. *Optics letters*, 28(4):272–274, 2003.
- [2] A. L. Huston and Jay D. Eversole. Strain-sensitive elastic scattering from cylinders. *Optics letters*, 18(13):1104–1106, 1993.
- [3] M Pöllinger, D. OShea, F. Warken, and A. Rauschenbeutel. Ultrahigh-Q tunable whispering-gallery-mode microresonator. *Physical review letters*, 103(5):053901, 2009.
- [4] M. Baaske, M. R. Foreman, and F. Vollmer. Single-molecule nucleic acid interactions monitored on a label-free microcavity biosensor platform. *Nature nanotechnology*, 9(11):933–939, 2014.
- [5] F. Vollmer and S. Arnold. Whispering-gallery-mode biosensing: label-free detection down to single molecules. *Nature methods*, 5(7):591–596, 2008.
- [6] F. Vollmer, D. Braun, A. Libchaber, M. Khoshsima, I. Teraoka, and S. Arnold. Protein detection by optical shift of a resonant microcavity. *Applied Physics Letters*, 80(21):4057–4059, 2002.
- [7] J. U. Fürst, D. V. Strekalov, D. Elser, M. Lassen, U. Andersen, Ch. Marquardt, and G. Leuchs. Naturally phase-matched second-harmonic generation in a whispering-gallery-mode resonator. *Physical review letters*, 104(15):153901, 2010.
- [8] J. U. Fürst, D. V. Strekalov, D. Elser, A. Aiello, U. Andersen, Ch. Marquardt, and G. Leuchs. Quantum light from a whispering-gallery-mode disk resonator. *Physical review letters*, 106(11):113901, 2011.
- [9] G. Schunk, U. Vogl, F. Sedlmeir, D. V. Strekalov, A. Otterpohl, V. Averchenko, H. Schwefel, G. Leuchs, and Ch. Marquardt. Frequency tuning of a triply-resonant whispering-gallery mode resonator to mhz wide transitions for proposed quantum repeater schemes. *arXiv preprint arXiv:1510.01198*, 2015.
- [10] M. Förtsch, J. U. Fürst, C. Wittmann, D. Strekalov, A. Aiello, M. V. Chekhova, C. Silberhorn, G. Leuchs, and C. Marquardt. A versatile source of single photons for quantum information processing. *Nature communications*, 4:1818, 2013.

- [11] B. Saleh and M. C. Teich. *Fundamentals of photonics*, volume 22. Wiley New York, 1991.
- [12] R. W. Boyd. *Nonlinear optics*. Academic press, 2003.
- [13] U. Schlarb, M. Wöhlecke, B. Gather, A. Reichert, K. Betzler, T. Volk, and N. Rubinina. Refractive indices of Zn-doped lithium niobate. *Optical Materials*, 4(6):791–795, 1995.
- [14] U. Schlarb and K. Betzler. Influence of the defect structure on the refractive indices of undoped and Mg-doped lithium niobate. *Physical Review B*, 50(2):751, 1994.
- [15] K. Wong. *Properties of lithium niobate*. Number 28. IET, 2002.
- [16] R. S. Weis and T. K. Gaylord. Lithium niobate: summary of physical properties and crystal structure. *Applied Physics A*, 37(4):191–203, 1985.
- [17] J. F. Nye. *Physical properties of crystals: their representation by tensors and matrices*. Oxford university press, 1985.
- [18] R. R. Birss et al. *Symmetry and magnetism*, volume 863. North-Holland Amsterdam, 1964.
- [19] R. T. Smith and F. S. Welsh. Temperature dependence of the elastic, piezoelectric, and dielectric constants of lithium tantalate and lithium niobate. *Journal of applied physics*, 42(6):2219–2230, 1971.
- [20] R. D. Richtmyer. Dielectric resonators. *Journal of Applied Physics*, 10(6), 1939.
- [21] <http://thetrimmierlife.com/2009/06/>.
- [22] P Féron. Whispering gallery mode lasers in erbium doped fluoride glasses. In *Annales de la Fondation Louis de Broglie*, volume 29, pages 317–329. Fondation Louis de Broglie, 2004.
- [23] S. P. Vyatchanin, M. L. Gorodetskii, and V. S. Il’Chenko. Tunable narrow-band optical filters with modes of the whispering gallery type. *Journal of Applied Spectroscopy*, 56(2):182–187, 1992.
- [24] D. V. Strekalov, R. J. Thompson, L. M. Baumgartel, I. S. Grudinin, and N. Yu. Temperature measurement and stabilization in a birefringent whispering gallery mode resonator. *Optics express*, 19(15):14495–14501, 2011.
- [25] T. Ioppolo, U. K. Ayaz, and M. V. Ötügen. High-resolution force sensor based on morphology dependent optical resonances of polymeric spheres. *Journal of applied physics*, 105(1):013535, 2009.
- [26] S. M. Spillane, T. J. Kippenberg, and K. J. Vahala. Ultralow-threshold Raman laser using a spherical dielectric microcavity. *Nature*, 415(6872):621–623, 2002.

- [27] G. Kozyreff, D. Juarez, and J. Martorell. Whispering-gallery-mode phase matching for surface second-order nonlinear optical processes in spherical microresonators. *Physical Review A*, 77(4):043817, 2008.
- [28] G. Schunk. *Quantum light fields from whispering-gallery resonators*. Master thesis, 2011.
- [29] A. Otterpohl. *Studies on optomechanics in a nonlinear crystalline whispering gallery mode resonator*. Master thesis, 2015.
- [30] G. Schunk, J. U. Fürst, M. Förtsch, D. V. Strekalov, U. Vogl, F. Sedlmeir, H. Schwefel, G. Leuchs, and C. Marquardt. Identifying modes of large whispering-gallery mode resonators from the spectrum and emission pattern. *Optics express*, 22(25):30795–30806, 2014.
- [31] A. N. Oraevsky. Whispering-gallery waves. *Quantum Electronics*, 32(5):377–400, 2002.
- [32] J. C. Knight, N. Dubreuil, V. Sandoghdar, J. Hare, V. Lefevre-Seguin, J. M. Raimond, and S. Haroche. Mapping whispering-gallery modes in microspheres with a near-field probe. *Optics letters*, 20(14):1515–1517, 1995.
- [33] M. L Gorodetsky and V. S. Ilchenko. Optical microsphere resonators: optimal coupling to high-Q whispering-gallery modes. *JOSA B*, 16(1):147–154, 1999.
- [34] F. Sedlmeir, R. Zeltner, G. Leuchs, and H. Schwefel. High-Q mgf 2 whispering gallery mode resonators for refractometric sensing in aqueous environment. *Optics express*, 22(25):30934–30942, 2014.
- [35] M. Förtsch. *Development of a versatile source of single photons*. PhD thesis, 2014.
- [36] G. Kozyreff, J. L. Dominguez-Juarez, and J. Martorell. Nonlinear optics in spheres: from second harmonic scattering to quasi-phase matched generation in whispering gallery modes. *Laser & Photonics Reviews*, 5(6):737–749, 2011.
- [37] V. S. Ilchenko, A. B. Matsko, A. Savchenkov, and L. Maleki. Low-threshold parametric nonlinear optics with quasi-phase-matched whispering-gallery modes. *JOSA B*, 20(6):1304–1308, 2003.
- [38] J. U. Fürst, D. V. Strekalov, D. Elser, A. Aiello, U. L. Andersen, Ch. Marquardt, and G. Leuchs. Low-threshold optical parametric oscillations in a whispering gallery mode resonator. *Physical review letters*, 105(26):263904, 2010.
- [39] A. Savchenkov, A. Matsko, V. Ilchenko, and L. Yu, N. and Maleki. Whispering-gallery-mode resonators as frequency references. ii. stabilization. *JOSA B*, 24(12):2988–2997, 2007.
- [40] M. Gorodetsky and A. Fomin. Geometrical theory of whispering-gallery modes. *Selected Topics in Quantum Electronics, IEEE Journal of*, 12(1):33–39, 2006.

- [41] T. Ioppolo and M. V. Ötügen. Pressure tuning of whispering gallery mode resonators. *JOSA B*, 24(10):2721–2726, 2007.
- [42] Matthew F. *Self coupling of WGMs and induced resonance shifts*. Internal communication, 2015.
- [43] <http://attocube.com/attomotion/premium-line/anpx101/>.
- [44] R. Gerson, J. F. Kirchhoff, L. E. Halliburton, and D. A. Bryan. Photoconductivity parameters in lithium niobate. *Journal of Applied Physics*, 60(10):3553–3557, 1986.
- [45] J. C. Janas. *Temperature stabilization of birefringent whispering gallery mode resonators*. Bachelor thesis, 2015.
- [46] M. Leidinger, S. Fieberg, N. Waasem, F. Kühnemann, K. Buse, and I. Breunig. Comparative study on three highly sensitive absorption measurement techniques characterizing lithium niobate over its entire transparent spectral range. *Optics express*, 23(17):21690–21705, 2015.
- [47] H. P. Wagner, H. Schmitzer, J. Lutti, P. Borri, and W. Langbein. Effects of uniaxial pressure on polar whispering gallery modes in microspheres. *Journal of Applied Physics*, 113(24):243101, 2013.

Declaration of originality

I, Navid Soltani, hereby declare that the composition of this thesis as well as the research reported herein represent my original work. Information from external sources has been acknowledged, the corresponding references are given in the text.

March 20, 2016

Navid Soltani